Journal of Structural Geology 134 (2020) 104013

Contents lists available at ScienceDirect

Journal of Structural Geology

journal homepage: http://www.elsevier.com/locate/jsg

Distinguishing coeval patterns of contraction and collapse around flow lobes in mass transport deposits

G.I. Alsop [a,*], R. Weinberger [b,c], S. Marco [d], T. Levi [b]

[a] Department of Geology and Geophysics, School of Geosciences, University of Aberdeen, Aberdeen, UK
[b] Geological Survey of Israel, Jerusalem, Israel
[c] Department of Geological and Environmental Sciences, Ben Gurion University of the Negev, Beer Sheva, Israel
[d] Department of Geophysics, Tel Aviv University, Israel

ARTICLE INFO

Keywords:
Mass transport deposit
Slump
AMS
Dead sea

ABSTRACT

Gravity-driven mass transport deposits (MTDs) form by the downslope-directed movement of sediment associated with slope failure. Simple models suggest that extension forms at the upslope (head) area, contraction is focussed in the downslope toe of the slump, while differential shear associated with strike-slip is restricted to the lateral margins of the slump. Although the head and toe are considered to be dominated by layer-parallel shear (LPS), differential layer-normal shear (LNS) may be generated around the lateral margins of slumps and potentially also within MTDs where flow has been separated into different 'lobes'. Despite this realisation that LNS must form, there has been little work into the geometries and spatial relationships of resulting structures. Using the late Pleistocene Lisan Formation exposed around the Dead Sea Basin as our case study, we examine detailed (<10 m) relationships of folds and thrusts created during LNS and LPS, as well as investigating the role of broadly coeval extension that may reactivate these structures. We also undertake analysis of anisotropy of magnetic susceptibility (AMS) fabrics to determine flow and shear relationships around folds and detachments created during LNS and LPS. Our study shows that LPS results in gently-curvilinear fold hinges that arc around the transport direction while LNS results in cylindrical fold hinges developed oblique or sub-parallel to transport. Such folds may be recumbent or upright, and associated with lateral ramps marking areas of differential LNS within the MTD. These structures are interpreted to accommodate variations in the amount and direction of downslope-directed movement resulting in LNS around the margins of individual flow 'lobes' that are developed over tens of metres. These 'lobes' display broadly down-slope transport with locally radial flow that results in along-strike shortening between lobes. Our analysis of AMS fabrics shows that they are controlled by slump folds, but magnetic fabrics do not differentiate how these folds were created in zones of LPS or differential LNS. AMS taken from gouge formed along detachments marked by differential LNS provide a first-order indicator for the transport direction. In addition, AMS fabrics in gouge or fluidised layers directly beneath thrust ramps, reveals prolate fabrics marking a component of strike-parallel flow along the branching intersections of thrust ramps and flats. Extensional faults directly reactivate existing thrusts, or create new extensional faults that are sub-parallel to thrusts or cut across them at steeper angles. Extension is part of the same MTD event as a sedimentary cap that is deposited out of suspension following slope failure, overlies and locally thickens into the hangingwall of extensional faults to create 'growth' sequences. Extensional reactivation and 'collapse' of original thrusts may help explain why contraction is apparently 'missing' from many seismic sections across MTDs.

1. Introduction

Slope failure results in the gravity-driven downslope movement of sediment that forms mass transport deposits (MTDs) across a range of scales and settings (e.g. Corredor et al., 2005; Zalan, 2005; Bull et al., 2009; Butler and Paton, 2010, de Vera et al., 2010; Van der Merwe et al., 2011; Morley et al., 2011; Jackson, 2011; Peel, 2014; Scarselli et al., 2016; Reis et al., 2016; Korneva et al., 2016). Simple models of MTDs interpret the upslope (head) region to be dominated by extension, while the downslope (toe) focusses contraction (e.g. Farrell and Eaton, 1987;

* Corresponding author.
E-mail address: Ian.Alsop@abdn.ac.uk (G.I. Alsop).

https://doi.org/10.1016/j.jsg.2020.104013
Received 15 July 2019; Received in revised form 11 February 2020; Accepted 11 February 2020
Available online 12 February 2020

Frey Martinez et al., 2005; Armandita et al., 2015; Fossen, 2016, p.388; Steventon et al., 2019) (Fig. 1). These areas of contraction and extension are separated by an intervening 'translational domain' (Fig. 1). Within classical models of MTDs, the extension in the upslope area should be equivalent to contraction in the downslope toe (e.g. Farrell, 1984; Gibert et al., 2005; Garcia-Tortosa et al., 2011), although this is rarely achieved with contraction apparently 'missing' when attempts are made to balance structures on seismic sections across MTDs (Butler and Paton, 2010; de Vera et al., 2010). The central 'translational' domain of the MTD is considered to undergo relatively little deformation, although the lateral margins are marked by differential shear associated with strike-slip displacement (e.g. Farrell, 1984) (Fig. 1). The dip-slip dominated extensional and contractional domains at the head and toe of the MTD are marked by relatively uniform displacement along the strike of the structure and therefore equate to layer-parallel shear (LPS), whereas the lateral margins are marked by pronounced along-strike variation in displacement that forms layer-normal shear (LNS) (Fig. 1). Relatively little detailed work has been undertaken on this LNS, perhaps reflecting the fact that transport-normal sections are required to best interpret it. However, differential LNS has been suggested to create transport sub-parallel folding within some MTDs (Farrell and Eaton, 1987; Alsop and Holdsworth, 2007; Debacker et al., 2009; Sharman et al., 2015; Sobiesiak et al., 2017; Jablonska et al., 2018). In addition, the development of secondary flow cells within MTDs related to variations in rates of downslope movement (e.g. Alsop and Marco, 2014) may also generate local areas of LNS within individual MTDs that separate different flow 'lobes'.

Seismic sections may be useful in determining the bulk geometry of large-scale MTDs developed in offshore areas (e.g. Scarselli et al., 2016; Steventon et al., 2019). However, their resolution generally prohibits the detailed analysis of subtle structural relationships on a smaller (<10 m) scale (e.g. see Jolly et al., 2016). Furthermore, seismic sections are typically less well constrained when interpreting steep to sub-vertical strike-slip features that may form in LNS-dominated areas around the lateral margins of MTDs (e.g. Debacker et al., 2009; Sharman et al., 2015). We have therefore attempted to circumvent some of these general issues by undertaking a detailed outcrop-based case study of a late-Pleistocene MTD in the Dead Sea Basin whose palaeo-geographic context is well understood. Within this case study, we analyse fold and thrust structures that developed in a MTD during retrogressive slope failure (i.e. thrusts get younger higher up the palaeoslope) while movement still continued on older thrusts i.e. synchronous thrusting (Alsop et al., 2018). Although the majority of studies into fold and thrust geometries analyse transport-parallel sections, significant information regarding the along-strike extent and interaction between adjacent thrusts may be gained from transport-normal sections (e.g. Farrell and Eaton, 1987; Alsop and Holdsworth, 2007; Debacker et al., 2009; Sharman et al., 2015; Sobiesiak et al., 2017; Jablonska et al., 2018). We therefore investigate transport-normal sections in order to establish the lateral interplay between thrusts and the nature of structures created to accommodate differential shear between the thrust systems in MTDs. We also employ Anisotropy of Magnetic Susceptibility (AMS) techniques which are generally used to characterise fabrics within rocks and sediments, and are here utilised to examine transport directions and the relationships between AMS and folding in areas of LPS and LNS. Our research aims to broadly address the following questions.

i) What fold patterns are created during layer-parallel and layer-normal shear in MTDs?
ii) How does transport direction vary in different flow lobes within an MTD?
iii) How do thrust systems interact with one another in MTDs?
iv) Can AMS fabrics be used to distinguish transport-parallel and transport-normal folds?
v) Could extensional reactivation of thrusts conceal 'missing' contraction in MTDs?

2. Layer-parallel and layer-normal shear in MTDs

Within metamorphic thrust sheets, deformation has long been interpreted in terms of layer-parallel shear (LPS), where displacement is broadly uniform along the strike of the thrust plane, and layer-normal shear (LNS), where variable along-strike displacement is accommodated via transport-parallel folding and shear across a variety of scales (e.g. Fischer and Coward, 1982; Coward and Potts, 1983; Alsop and Holdsworth, 1993; Xypolias and Alsop, 2014). Many of the structural

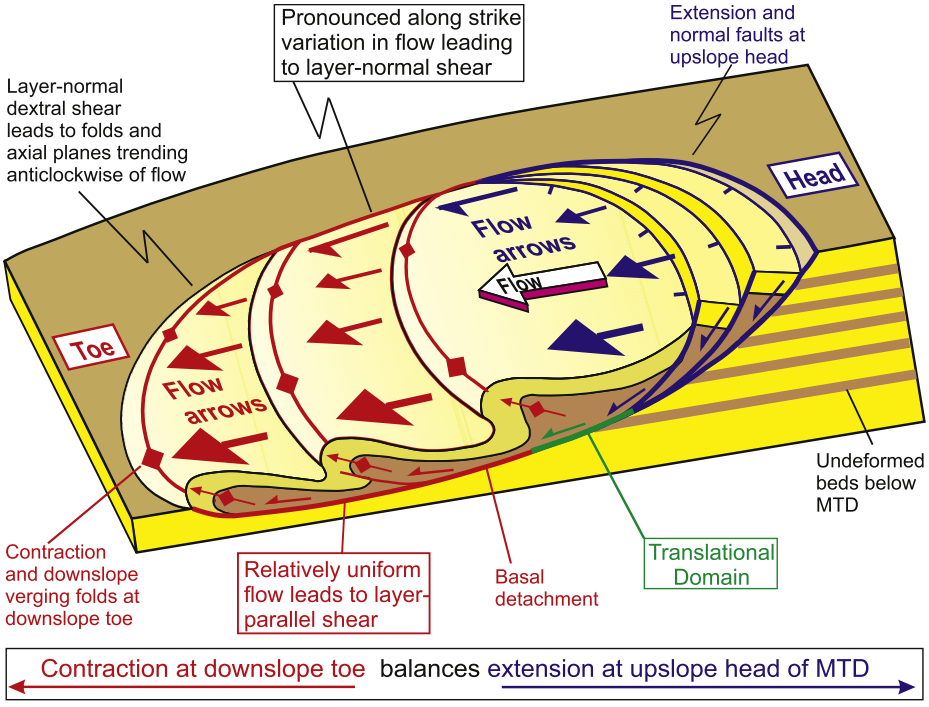

Fig. 1. Schematic summary cartoon of gravity-driven slope failure associated with mass transport deposits (MTD) where downslope contraction at the toe (in red) is broadly balanced by extension in the upslope head domain (in blue). Areas of contraction and extension are separated by an intervening translational domain (in green) in which deformation is less pronounced. Flow (shown by arrows) is relatively uniform in the central area resulting in layer parallel shear (LPS), whereas it becomes more variable towards the lateral margins of the MTD resulting in differential layer normal shear (LNS). (For interpretation of the references to colour in this figure legend, the reader is referred to the Web version of this article.)

observations and relationships observed within metamorphic thrusts may be equally applied to MTDs (e.g. Alsop and Holdsworth, 2007). Where flow along a detachment within an MTD has a relatively uniform velocity along strike then it is associated with LPS (Figs. 1 and 2a). This results in gently-curvilinear, non-cylindrical fold hinges that form at high angles to the flow direction and verge downslope (Figs. 1 and 2a) Associated axial planes strike at high angles or normal to the flow direction and generally dip up the slope (e.g. Woodcock, 1976a, b: 1979) (Fig. 2a). Axial planes linked to S and Z folds with opposing vergence, such as created around back folds and thrusts, generally intersect one another at high angles or normal to the flow direction. With continued progressive deformation, fold hinges may rotate towards the flow direction to create curvilinear sheath folds Although rotation of folds results in variable hinge trends, their associated axial planes simply tilt and flatten into the sub-horizontal shear plane, meaning that axial planar strikes will not significantly vary during LPS (see Alsop and Carreras, 2007 for a review of sheath folds). The normal to axial-planar strikes (i.e. the trend of the 'trail' of poles on a stereonet) will thus align along the mean flow direction and form a reliable indicator of LPS transport (Fig. 2a).

Where flow along a detachment within an MTD has a variable velocity along strike then this creates differential displacement associated with LNS (Figs. 1 and 2b). This results in cylindrical folds that form oblique (<45°) or sub-parallel to the flow direction, and verge at high angles to the slope (Figs. 1 and 2b). When viewed towards the flow direction, differential dextral shear generates S fold hinges and axial planes that trend anticlockwise of flow, whereas differential sinistral shear creates Z fold hinges and axial planes that trend clockwise of flow

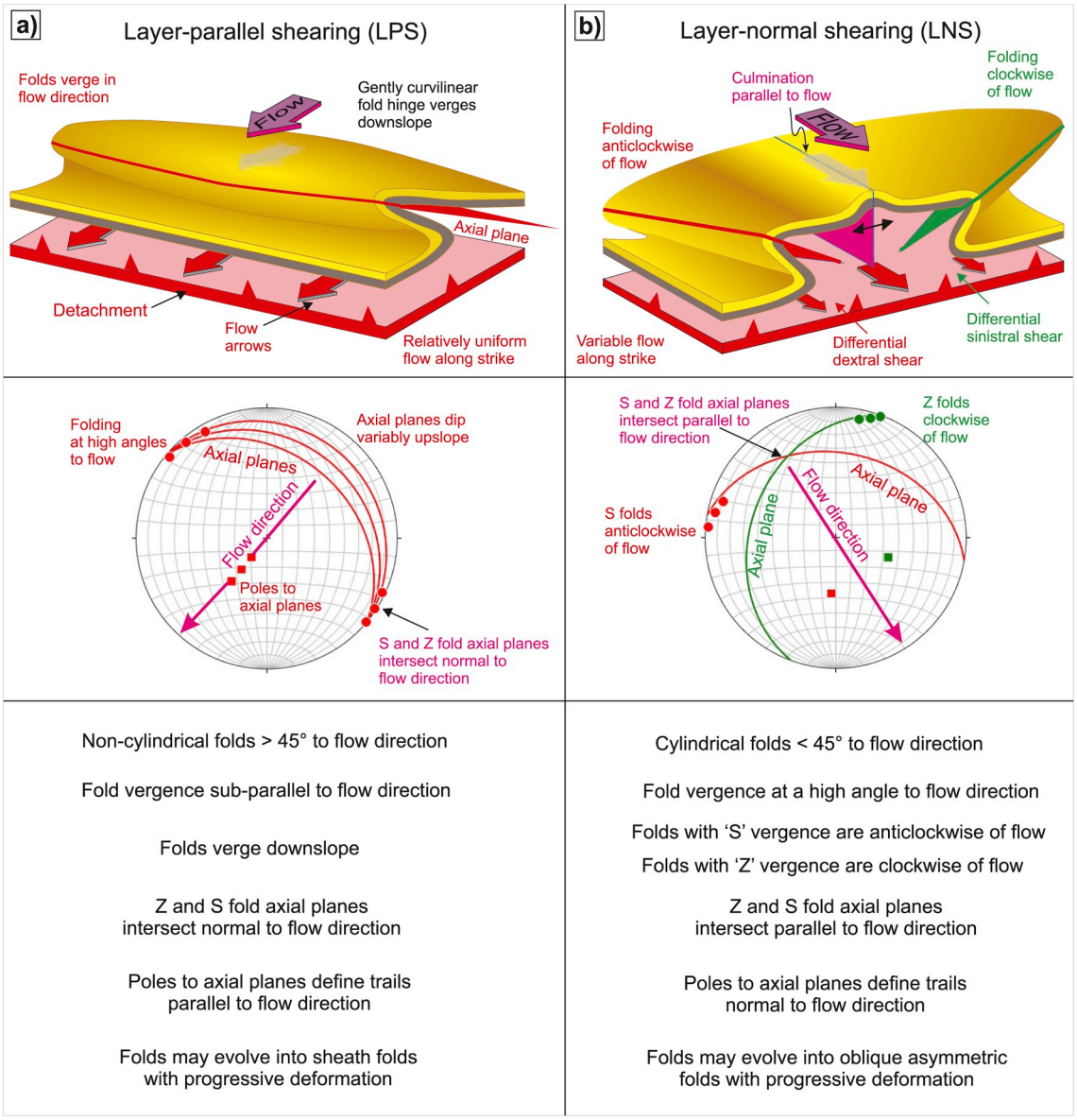

Fig. 2. Summary figure highlighting fold geometries, schematic stereonet patterns and significant relationships associated with flow perturbation folding in MTDs. a) Layer-parallel shearing (LPS) is marked by relatively uniform flow velocity along strike resulting in downslope verging folds forming at high angles to flow. Associated stereonet shows fold hinges (red circles) and axial planes (red great circles) that dip variably upslope resulting in a 'trail' of poles (red squares) that lie parallel to the flow direction. b) Layer-normal shearing (LNS) is marked by variable flow velocity along strike as represented by different sized flow arrows. Differential dextral shear generates anticlockwise trending folds, whereas sinistral shear is associated with folds trending clockwise of flow. Associated stereonet shows axial planes of Z and S folds (in green and red respectively) dipping towards one another intersecting parallel to the flow direction. Apart from red and green colours for S and Z folds respectively, stereonet symbols are the same as Fig. 2a. See text for further detail. (For interpretation of the references to colour in this figure legend, the reader is referred to the Web version of this article.)

(Fig. 2b). Axial planes linked to the variably orientated S and Z folds will generally intersect one another parallel to the flow direction, with the intersection marking the upslope vector (due to axial planes generally dipping up the palaeoslope) (Fig. 2b). With continued progressive deformation, fold hinges may undergo only limited rotation towards the flow direction, as increasing values of shear strain are required to rotate sub-parallel hinges into flow, and oblique asymmetric folds with stretching along hinges may be produced (e.g. Coward and Potts, 1983). Axial planes also lack significant rotation and folds therefore maintain high angles of cut-off with the underlying detachment surface. Any variability in axial planar orientation results in poles only displaying limited 'trails' at high angles to flow, and 'clustered' patterns are more

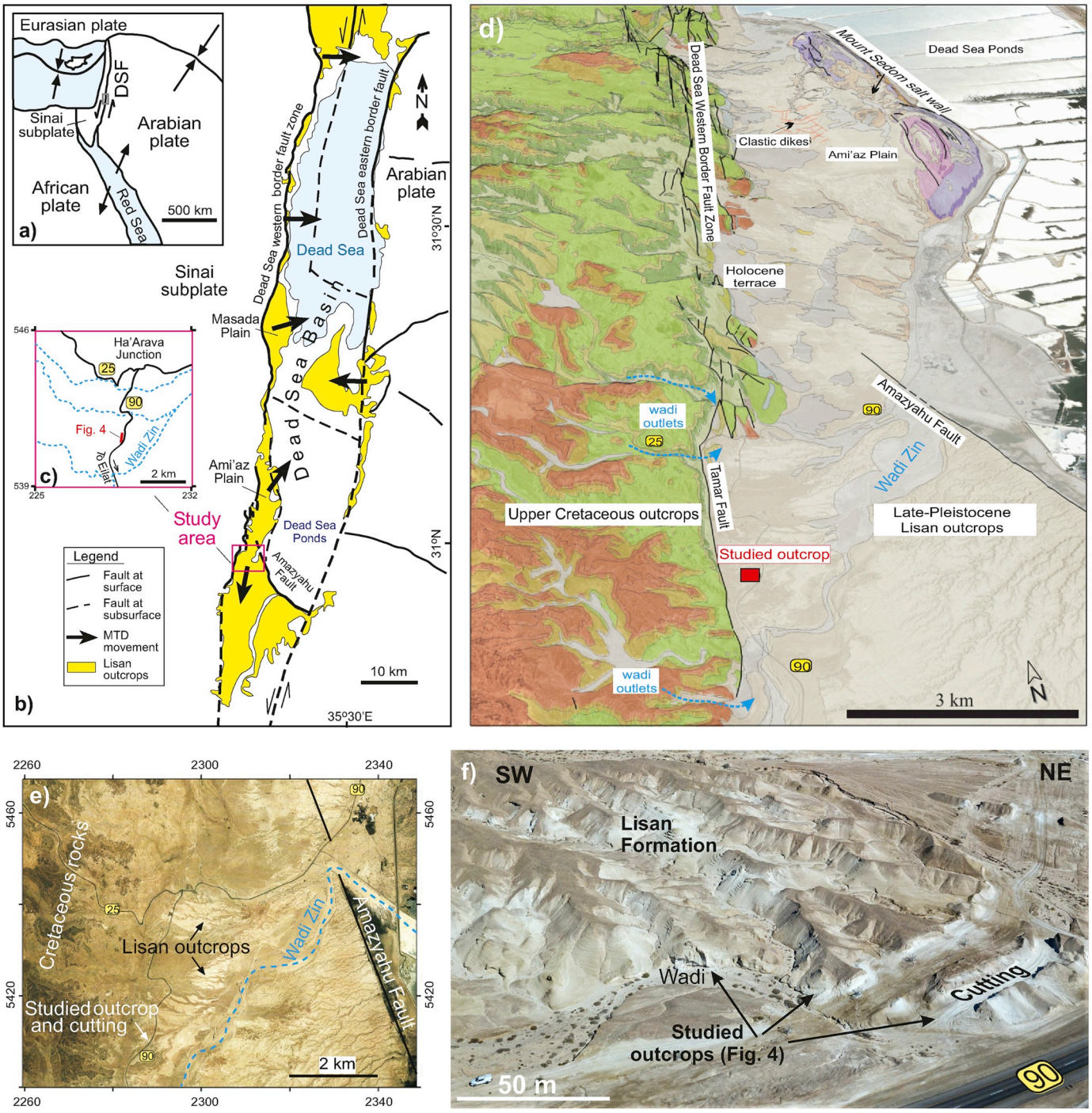

Fig. 3. a) General map showing tectonic plates in the Middle East and the location of the Dead Sea Fault (DSF). b) Map of the Dead Sea showing the position of the Wadi Zin case study area (red box) (based on Sneh and Weinberger, 2014). c) Inset locality map showing details of the cutting and outcrops that form the Zin case study area (Fig. 4) relative to Highways 25 and 90. d) Perspective view (looking North) of a geological map draped on a Google Earth image of the southern Dead Sea Basin. Upper Cretaceous (greens and browns) outcrops to the west of the Dead Sea Western Border Fault Zone, while Lisan Formation (buff colour) outcrops to the east. Geology is after Sneh et al. (1998) and Agnon et al. (2006b). e) Image of the light-coloured Lisan Formation at Wadi Zin, with the brownish Cretaceous rocks to the west and the trace of the Amazyahu Fault to the east. Coordinates of the Israel national grid are shown. f) Aerial drone photograph showing the case study outcrops and cutting within the Lisan Formation immediately to the west of Highway 90. The 4WD vehicle at the bottom left of the photo helps provide a scale. (For interpretation of the references to colour in this figure legend, the reader is referred to the Web version of this article.)

typical on stereonets. In general, steeper axial planes in both LPS and LNS settings are more reliable indicators of palaeoflow, as they have typically suffered less rotation during subsequent progressive shearing (Alsop and Marco, 2012a; Alsop et al., 2016).

3. Regional setting

The Dead Sea Fault system has been active since the Early to Middle Miocene and comprises two parallel, left-stepping, sinistral fault strands that bound the pull-apart Dead Sea Basin (e.g. Bartov et al., 1980 Garfunkel, 1981; Garfunkel and Ben-Avraham, 1996; Nuriel et al., 2017) (Fig. 3a and b). Numerous earthquakes along this fault system triggered co-seismic deformation (e.g. Agnon et al., 2006a,b; Weinberger et al., 2016) together with soft-sediment deformation and MTDs (e.g. El-Isa and Mustafa, 1986; Marco et al., 1996; Alsop and Marco, 2011, 2014; Alsop et al., 2020a) in the late-Pleistocene Lisan Formation (70–15 ka) (Haase-Schramm et al., 2004).

The Lisan Formation comprises a sequence of alternating detrital-rich and aragonite-rich laminae on a sub-mm scale (e.g. Ben Dor et al., 2019). They represent annual varve-like cycles with winter flood events washing clastic material into the lake to create the detrital-rich laminae, while hypersaline waters precipitated aragonite-rich laminae in the hot dry summers (Begin et al., 1974). Counting of these varves when combined with isotopic dating suggests that the Lisan Formation was deposited at an average rate of ~1 mm per year (Prasad et al., 2009). The detrital units are mainly composed of quartz and calcite grains with minor feldspar, and clays (illite-smectite) (Haliva-Cohen et al., 2012). The thin detrital laminae display grain sizes of ~8–10 μm (silt), while the thicker detrital-rich beds are classified as very fine sands (60–70 μm) (Haliva-Cohen et al., 2012).

Based on clear stratigraphic correlation between fault slip events and layers of breccia, Marco and Agnon (1995) argue that the breccia layers are seismites. Alsop and Marco (2011) expand the recognition of seismites to slump sheets. Hence, the various types of MTDs within the Lisan Formation are considered to be triggered by $M > 5.5$ earthquakes along the Dead Sea Fault (Marco and Agnon, 1995; Marco et al., 1996; Lu et al., 2017), that also result in characteristic gravity-driven folds (e.g. Alsop et al., 2019, 2020b, c) and thrust systems in the MTDs (Alsop and Marco, 2011; Alsop et al., 2017a, b). The seismic-triggered shear between the lakebed and the overlying water body helps govern the evolution of the MTD deformation from linear waves through asymmetric billows, coherent vortices, and fully turbulent breccia (Heifetz et al., 2005; Wetzler et al., 2010). Individual MTDs are typically <1.5 m thick and are capped by undeformed horizontal beds of the Lisan Formation that locally erode the underlying fold and thrust systems, indicating that they formed at the sediment surface. The position of basal detachments beneath MTDs are controlled by variable lithologies and potentially fluid pressure (e.g. Alsop et al., 2016, Alsop et al., 2017a). Individual MTDs are vertically stacked and separated from one another by intervening undeformed beds, such that sections through the Lisan Formation comprise multiple alternations of MTDs and pristine packages of aragonite and detrital-rich laminae (see description in Alsop et al., 2016).

The MTDs around the Dead Sea Basin are developed on very gentle slopes of <1° dip and define an overall regional pattern of radial slumping directed towards the depo-centre of the present Dead Sea Basin (Alsop and Marco, 2012a, 2013), while MTDs on the eastern side of the Dead Sea are transported towards the west (El-Isa and Mustafa, 1986) (Fig. 3b). Drill cores taken from the depo-centre of the Dead Sea reveal that the stratigraphic thickness of the Lisan Formation is three times greater than its onshore equivalent, largely due to the input of numerous MTDs from around the margins of the basin that accumulate in the depo-centre. (Lu et al., 2017; Kagan et al., 2018).

The Zin case study area (N30°57′38″ E35°18′9″) is positioned immediately to the west of Highway 90 and NW of Wadi Zin (Fig. 3c–f). It is located between the N–S trending Dead Sea western border fault zone with its southern continuation, the Tamar Fault, bounding the Cretaceous basin margin ~1 km to the west, and the NW-SE trending Amazyahu Fault ~5 km further NE (Fig. 3b,-f). As the Lisan Formation of the study area is positioned between major wadi outlets cutting the Cretaceous (Fig. 3d), it contains less detrital input that typically forms fans deposited from flood events emanating from these wadis. This area is ideal for the present case study concerning deformation in MTDs as it is well exposed at outcrop of the upper "White Cliff" section of the Lisan Formation, dated at 31–15 ka (Torfstein et al., 2007). No significant overburden was ever deposited above the Lisan Formation of the study area, meaning that structures are preserved with pristine geometries unaffected by compaction. Most of the observations are made along easily-accessible man-made cuttings that collectively form sections at right angles to one another (Fig. 3c, e, f, 4a). Numerous fluidised clastic dykes cut the deformed MTDs in the Lisan Formation (e.g. Porat et al., 2007; Levi et al., 2008), suggesting that it was fluid-saturated at the time of deformation (see Alsop et al., 2020b), while the present fluid content is still ~ 25% (Arkin and Michaeli, 1986; Frydman et al., 2008). At the time of deformation, sediments of the Lisan Formation were below storm wave base, with water likely to have been between 30 m and 100 m deep (Alsop and Marco, 2012b).

Our previous structural analysis demonstrates that a south-directed fold and thrust imbricated sequence formed within the case study (Alsop et al., 2018) (Fig. 4a). This south-verging MTD is directed away from the Dead Sea depocentre, and clearly does not form part of a radial pattern of slumping developed further north (Alsop and Marco, 2012a) (Fig. 3b) This apparently anomalous situation is explained by tilting of large-scale fault blocks associated with the transverse NW-SE trending Amazyahu Fault, which was active during deposition of the Lisan Formation and is developed immediately to the NE of the study area (Fig. 3b, d, e) (Smit et al., 2008; Weinberger et al., 2017). Gentle tectonic tilting of fault blocks by just a few degrees across this NE-dipping fault system (Smit et al., 2008) would be sufficient to alter directions of slope failure and gravity-driven MTD emplacement during deposition of the Lisan Formation (Alsop and Marco, 2012a, 2013).

4. Orientation and geometry of structures generated during LPS

Previous observations from the imbricated sequence exposed in the cutting in the eastern part of the study area (Fig. 4a, b, c) show that fold hinges and related axial planes trend broadly parallel to the strike of the associated thrust planes and at high angles to the flow direction (Alsop et al., 2018). In addition, correlation of individual thrusts across each side of the 10 m wide cutting suggest that displacement may only vary by ~1 m, thereby supporting the 1:10 along-strike gradients frequently termed the 'bow and arrow' rule of Elliot (1976) (quoted in Butler and McCaffrey, 2004 p. 916). These observations suggest that deformation is here dominated by LPS (Figs. 4d, 5a-h) (Alsop and Holdsworth, 1993, 2007).

In detail, forethrusts are E-W striking and dip gently towards the north, while associated fold hinges are sub-horizontal and typically trend E-W (Fig. 4a, e-h, 5a-d) (Alsop et al., 2018: Weinberger et al., 2017). The overall fold vergence is towards the south and west (shown in red in Fig. 4a). We use various methods to determine the flow direction, including the normals to mean fold hinge trends and axial-planar strikes (Alsop et al., 2018), and calculate that the flow direction is towards the south or SSW (Figs. 4 and 5). The fold and thrust system exposed in the trench cutting defines a classic overstep sequence where younger thrusts have developed above older thrusts (Alsop et al., 2018). The effect of this is for the thrust system to get progressively younger in the upslope direction towards the north. In addition, the amount of thrust displacement along thrusts progressively diminishes towards the north, suggesting that older thrusts continued to move during synchronous thrusting (Alsop et al., 2018).

Approximately 50 m further to the southwest, the same MTD deforms the same stratigraphy with a distinctive ~10 cm thick brown

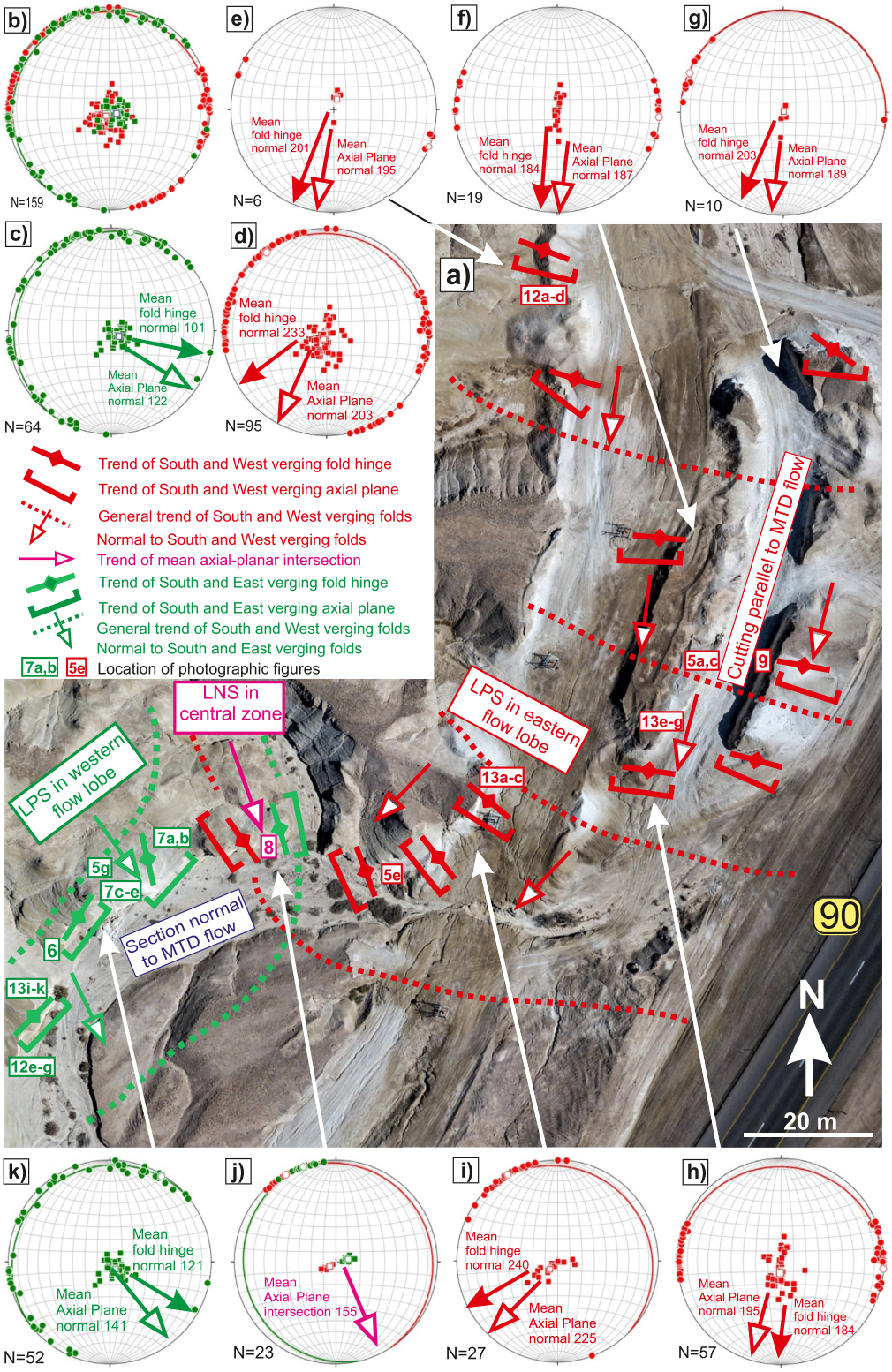

Fig. 4. a) Aerial drone photograph showing study area with south and west verging fold data (red data) and south and east verging fold data (in green). Refer to Fig. 3 for location of study area. Stereonets of b) overall fold data, c) fold data from south and east verging folds; d) fold data from south and west verging folds. Stereonets shown in e) – k) show fold data from specific areas (arrowed). In each case, fold hinges (solid circles), mean fold hinges (open circles), poles to axial planes (solid squares), mean pole to axial plane (open square) and normal to mean fold hinges and axial planes (arrows) are shown. On stereonets, solid arrows represent the normal to mean fold hinges and open arrows represent the normal to mean axial-planar strike. In j), the trend of mean axial planar intersections are shown by a purple arrow that corresponds with the purple transport arrow shown in a). Position of photograph localities shown in other figures are also shown on Fig. 4a. (For interpretation of the references to colour in this figure legend, the reader is referred to the Web version of this article.)

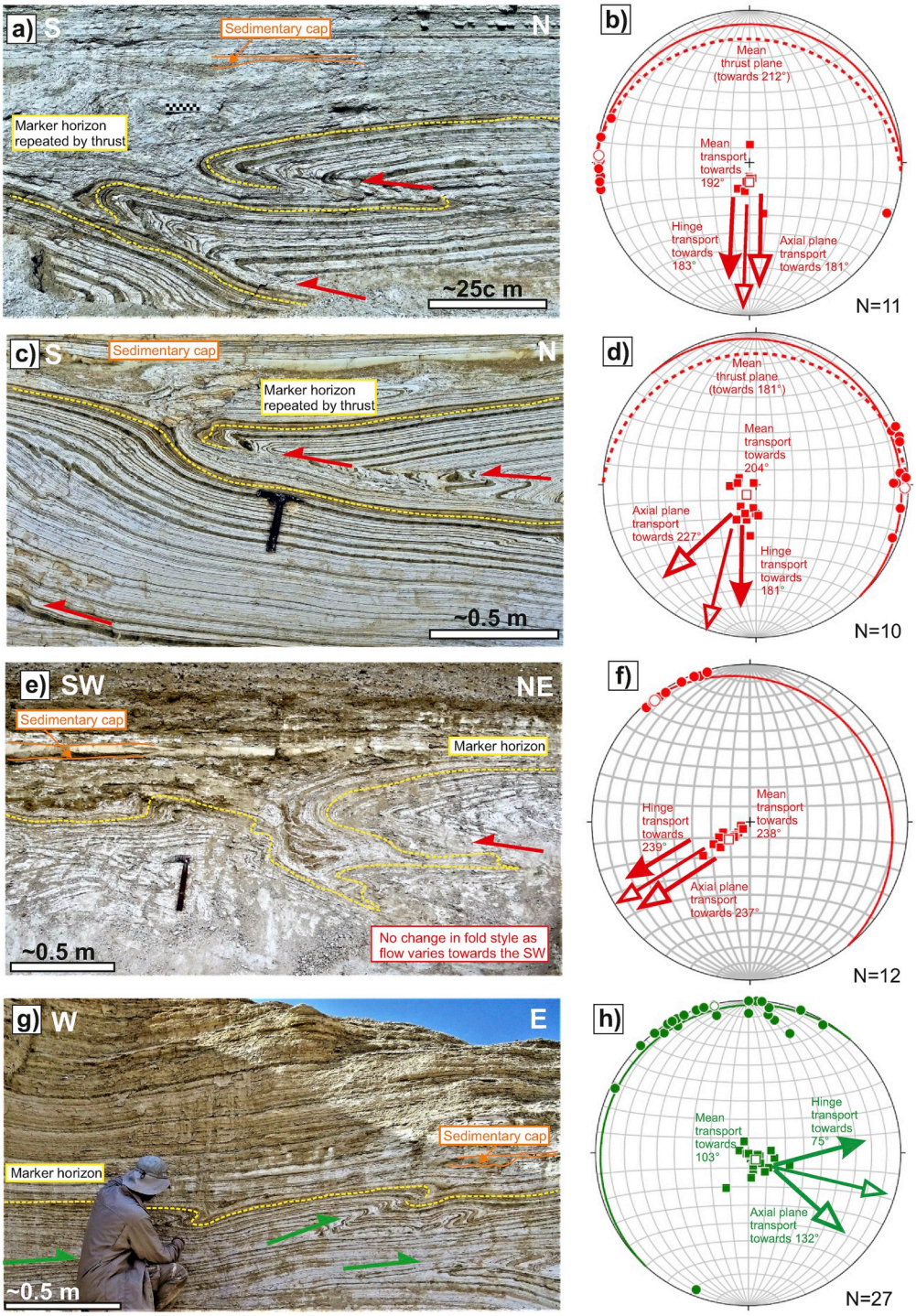

Fig. 5. Paired photographs and associated stereonets of folds and axial planes created during layer parallel shear (LPS) from both the eastern (a–f) and western flow lobes (g–h) (N30°57′38″ E35°18′9″) (see Fig. 4a). A distinctive 10 cm thick detrital marker horizon is highlighted (in yellow), while a sedimentary capping layer deposited from suspension following the slump is shown in orange. Photograph (a) and associated stereonet (b) of imbricated south-verging thrusts and folds (N = 11) developed within the Lisan Formation on the east side of the flow-parallel cutting (see Fig. 4a). b) Photograph (c) and associated stereonet (d) of thrust planes and folds (N = 10), showing fold hinges (mean 3/091), axial planes and thrust planes (mean 104/10 N) from the west side of the flow-parallel cutting (see Fig. 4a). Photograph (e) and associated stereonet (f) of SW-verging folds and thrusts from location shown on Fig. 4i. Stereonet (f) displays a prominent axial planar 'trail' of poles that is parallel to the flow direction. Photograph (g) and associated stereonet (h) showing SE-verging folds and thrusts from the western flow lobe (near location shown on Fig. 4k). Structural data on the stereonets are represented as follows: fold hinges (solid red/green circles), mean fold hinge (open red/green circle), poles to fold axial planes (solid red/green squares), mean pole to fold axial planes (open red/green squares), thrust planes (red great circles), and poles to thrust planes (solid red squares). On stereonets, solid arrows represent the normal to mean fold hinges and open arrows represent the normal to mean axial-planar strike. The small open arrows represent the calculated flow directions based on averaging the combined fold hinge and axial-planar data. (For interpretation of the references to colour in this figure legend, the reader is referred to the Web version of this article.)

marker layer, and the basal detachment developed immediately below a ~5 cm thick dark green detrital-rich layer as observed in the transport-parallel cutting (see Alsop et al., 2018). The outcrop is marked by SW verging folds that display a 30°–40° clockwise swing in trend compared to the cutting (Fig. 4a,i, 5e, f). The normal to fold hinges trends 240°, while the normal to associated axial planes is towards 225° suggesting that flow is towards the SW (Fig. 4a, i, 5e, f). The style of deformation is marked by recumbent to upright folds, resulting in variably dipping axial planes and 'pole trails' on stereonets, but is otherwise unchanged from observations in the transport-parallel cutting (Fig. 4).

In the extreme western part of the study area, the same MTD which deforms the distinctive ~10 cm thick brown marker layer is well exposed by the wadi and display south and east verging folds (Fig. 4a, b, c). Fold hinges are sub-horizontal to gently plunging and displays an arc of orientations varying from NE to NW trending, although the majority are orientated NE-SW (Fig. 4k). Axial planes are gently dipping and variably striking, with the mean dipping gently towards the NW and the normal to axial-planes trending between 132° and 141° (Figs. 4k and 5g, h). The overall fold vergence is towards the south and east (shown in green in Fig. 4a).

Within individual localities, the sub-horizontal fold hinges trend NE-SW and verge towards the SE, while their associated axial planes dip

gently towards the NW (Fig. 6a–d). The fold hinges trend parallel to the strike of their axial planes, and are gently curvilinear (22° variation along the hinge) about the inferred transport direction towards the SE (Fig. 6). Parasitic folds are also gently curvilinear about the inferred transport towards the SE (Fig. 6e and f). Gentle curvilinearity of fold hinges is consistent with LPS (Figs. 1 and 2a) and with continuing progressive deformation that would ultimately lead to the development of intensely curvilinear sheath folds.

5. Orientation and geometry of structures generated during LNS

Layer normal shear (LNS) is marked by pronounced displacement gradients along strike and results in transport sub-parallel folds with opposing vergence depending on the sense of differential shear (Figs. 1 and 2b). Approximately 100 m further southwest from the flow-parallel cutting shown in Fig. 4a, a WSW-ENE section normal to MTD transport reveals a series of folds and thrusts that deform the same stratigraphic package and detrital marker horizons as described previously (Figs. 4, 5 and 7a, b). This deformed horizon is overlain by the same sedimentary cap and is attributed to the same MTD event (Fig. 7a and b). Within this section, a series of both east and west dipping thrust ramps enclose fault-bounded horses that detach on the underlying basal detachment (Fig. 7a and b). We interpret these as lateral ramps that cut across footwall folds that verge towards the east. The angle of footwall cut-off is significantly greater than observed beneath thrust ramps in the LPS-dominated areas (Fig. 7c, d, e).

The section displays both recumbent and upright fold hinges that detach on underlying thrusts (Fig. 8a and b). Fold hinges have a mean trend of 340°–160° and are marked by reversals in fold vergence to define 'double-vergence' fold geometries (Fig. 8a, c, d, e), Folds associated with double-vergence have a recumbent attitude and are marked by class 1 to class 2 fold geometries (see Fossen, 2016) (Fig. 8a, b, d, f), Detrital-rich beds, such as the yellow marker bed, display more parallel (class 1) fold styles associated with greater relative competency compared to the aragonite-rich layers (see Alsop et al., 2020c for a full description). Variable double-vergence folding results in axial planes that dip and face in opposing directions and form a 155° (SSE) trending intersection (Fig. 8c, e). This is parallel to the calculated transport direction using the Axial-planar Intersection Method (AIM) of Alsop and Holdsworth (2007) (see also Alsop and Marco, 2012a; Alsop et al., 2016). MTD flow towards the SSE is broadly similar to the southerly transport direction calculated in the adjacent transport-parallel cutting (Fig. 4b, c, d) (Alsop et al., 2018). Within the 'double vergence' fold package, south and west verging fold hinges and associated axial planes generally trend anticlockwise of 340°, whereas south and east verging hinges are clockwise of 340°/160° that marks transport direction (Fig. 8e). There is no evidence of refolding of the opposing vergence folds and they are considered to be the same age. However, folds associated with the T2 thrust locally refold folds linked to the T1 thrust confirming this specific age relationship (Fig. 8b). The sedimentary cap thins over the crest of the double-vergence fold geometry indicating that this culmination resulted in thickening of the MTD and formed a relative structural 'high' when compared to the adjacent section (Fig. 8a, d). Hangingwall cut-offs above the thrust planes are at extremely high angles (~90°), while the thrust planes themselves are generally flat-lying within this transport-normal view (Fig. 8f and g). Locally, lateral ramps are developed that are associated with branching of the thrust system, together with thrust repetition of hangingwall stratigraphy and hangingwall folds (Fig. 8a, h). Within the WSW-ENE (070°) trending transport-normal section, overlying thrusts deform and refold structures related to underlying thrusts (Fig. 8a and b), thereby supporting the overstep thrust sequence even in this LNS-dominated setting (Fig. 8a and b). This is especially the case along lateral ramps where the underlying T1 thrust ramps up to join the overlying T2 thrust (Fig. 8a, h). Where hangingwall stratigraphy is cut across at high angles by thrusts, thin (<20 mm) zones of gouge are developed similar to that observed in transport-parallel sections (Fig. 8g). The gouge zones also correspond to high angles of hangingwall cut-off along basal detachments in the LNS sections (Fig. 8f and g).

6. Analysis of AMS fabrics

6.1. AMS methodology

The analysis of anisotropy of magnetic susceptibility (AMS) is used to characterise magnetic fabrics and internal deformation within rocks and sediments (e.g., Parés, 2015). The maximum K_1, intermediate K_2 and minimum K_3 magnetic susceptibility axes correspond to k_1, k_2 and k_3 eigenvalues of the AMS. The K_1 and K_3 axes are generally parallel to the long and short axes of particle shapes, respectively. When deposited in still-water, elongate particles tend to lie parallel to the horizontal bedding plane, forming a 'deposition fabric'. In this fabric, the K_1 and K_2 axes lie within the bedding plane and are indistinguishable, while the K_3 axes are vertical and well-clustered. During later soft-sediment deformation (see Maltman, 1984 for definitions), the original fabric might evolve into a 'deformation fabric', in which the K_1 and K_2 axes are well-clustered and clearly distinguishable. AMS has previously been used to determine the direction of MTD movement within the Lisan Formation, with the K_1 axes aligned with the orientation of fold hinges, and K_3 axes parallel to the poles of associated axial planes (Weinberger et al., 2017).

The AMS was studied at the Geological Survey of Israel rock-magnetic laboratory. The AMS was measured with a *KLY-4S* Kappabridge (AGICO Inc.) where the principal susceptibility axes with their 95% confidence ellipses (Jelinek, 1981) were analysed with *Anisoft42*. Mean susceptibility ($k_m = k_1 + k_2 + k_3/3$), degree of anisotropy ($P = k_1/k_3$), shape of the AMS ($T = (2lnk_2 - lnk_1 - lnk_3)/(lnk_1 - lnk_3)$, magnetic foliation ($F = k_2/k_3$) and magnetic lineation ($L = k_1/k_2$) were calculated according to Jelinek (1981). We analysed the magnetic fabrics of 122 samples from folds in both the LPS and LNS domains, gouge zones, secondary thrusts and basal detachment. The aragonite and the detritus layers of the Lisan Formation are diamagnetic and paramagnetic, respectively, while the bulk AMS susceptibility is typically positive. Titanomagnetite, magnetite, and greigite are the ferromagnetic carriers in the detrital laminae (e.g., Ron et al., 2006; Levi et al., 2006a, 2014).

6.2. AMS fabrics created during LPS

6.2.1. AMS fabrics created during LPS folding

Following Weinberger et al. (2017), we have undertaken AMS fabric analysis in folds and thrusts generated during LPS associated with southward-directed transport of MTDs (Alsop et al., 2018) (Figs. 4 and 9a, b). The AMS fabrics of the deformed layers are characterized by a "deformation fabric", with the K_1 and K_2 axes displaying well-defined sub-horizontal clusters, while K_3 are off vertical and show a trail of axes (Fig. 9c). The K_1 axes and fold hinges broadly coincide with one another (compare Fig. 9b and c), while K_3 axes and poles to axial planes also broadly correspond (compare Figs. 4h, 5d and 9b with 9c). Magnetic fabrics from around folds suggests movement broadly towards the South (167°) (Fig. 9c and d) and this is similar to transport directions calculated from the normals to thrust planes (175°), fold hinges (173°) and axial planes (215°) (Fig. 9b) providing a bulk flow towards ~190° (Fig. 4a, h).

6.2.2. AMS fabrics created during LPS shearing

We sampled a thick (3 cm) unit of gouge that is developed along the basal detachment immediately beneath a forethrust and backthrust intersection within the LPS cutting (Fig. 9a, e, f). The transport directions calculated from the normals to thrust planes (196°), fold hinges (172°) and axial planes (190°) (Fig. 9g) suggest a bulk flow towards ~186° (Fig. 9g) which is similar to directions calculated in the adjacent LPS fold

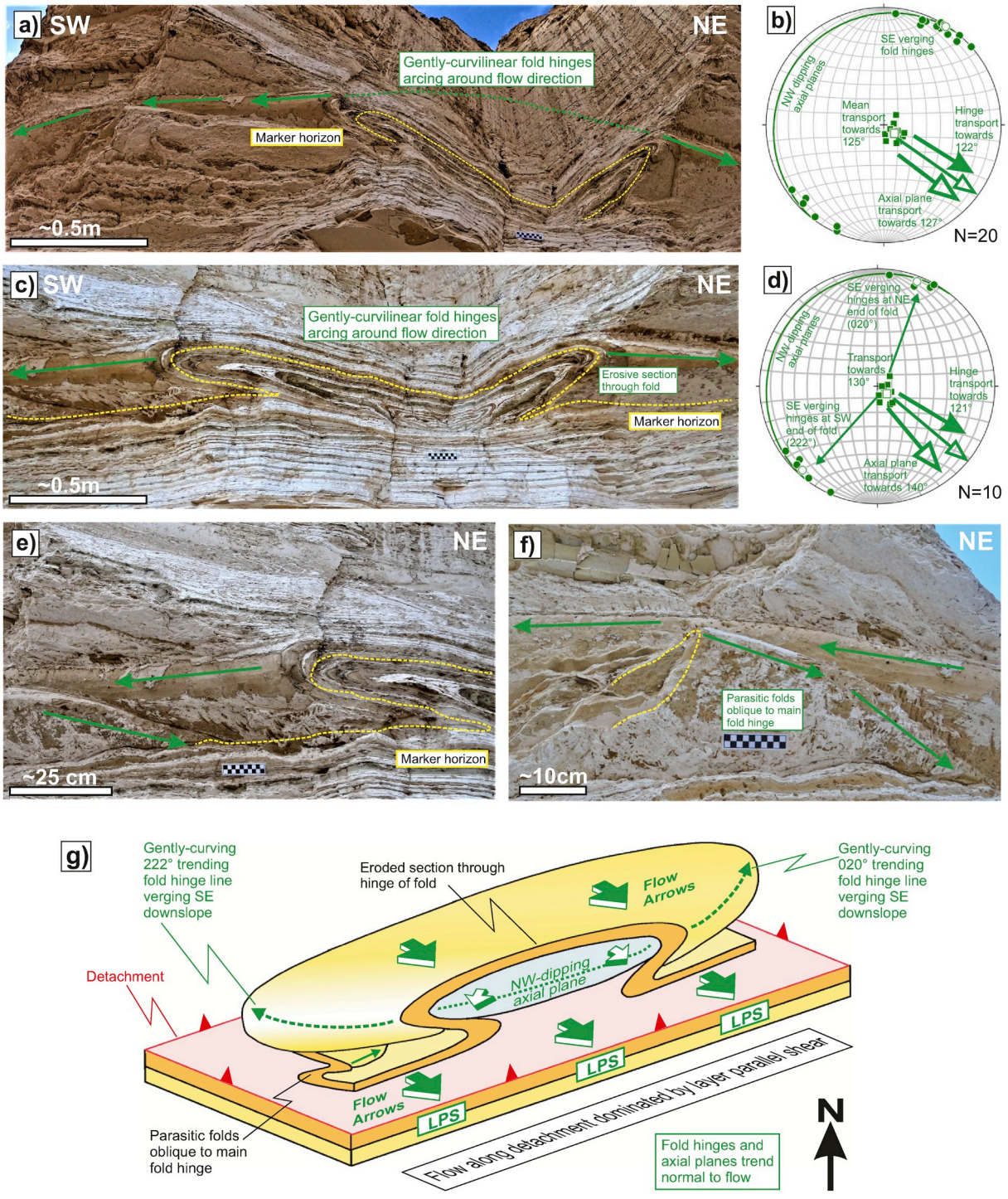

Fig. 6. a) Photograph and associated stereonet (b) of now eroded section through a gently curvilinear hinge defined by the distinctive 10 cm thick detrital marker horizon (highlighted in yellow). The fold (viewed from below) is created by LPS in the western flow lobe located by Fig. 4k. c) More detailed photograph of the fold in the overhang, together with (d) structural data from the folded marker horizon. Photographs e) and f) show a close-up of the southwestern hinge, together with the associated parasitic hinge that plunges in an opposing direction. g) Schematic summary cartoon of the fold shown in (a) interpreted to reflect a gently-curvilinear fold generated during LPS. Structural data on the stereonets (b, d) are represented as follows: fold hinges (solid green circles), mean fold hinge (open green circle), poles to fold axial planes (solid green squares), mean fold axial planes shown as a green great circle and the associated pole as an open green square. On stereonets, solid arrows represent the normal to mean fold hinges and open arrows represent the normal to mean axial-planar strike. The small open arrows represent the calculated flow directions based on averaging the combined fold hinge and axial-planar data. (For interpretation of the references to colour in this figure legend, the reader is referred to the Web version of this article.)

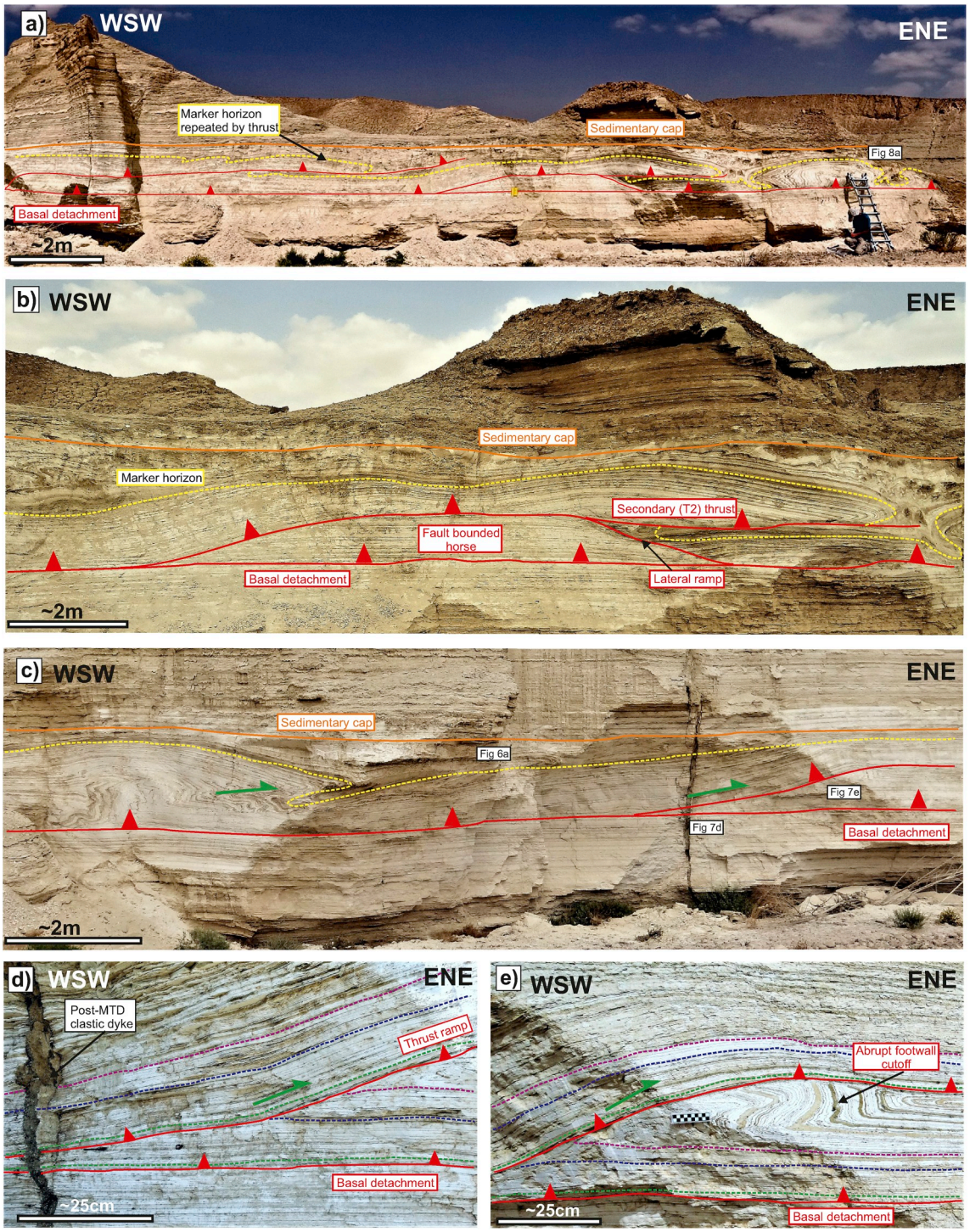

Fig. 7. a) Overview of transport-normal section showing distinctive 10 cm thick detrital marker horizon (highlighted in yellow) with increasing LNS structures towards the ENE. b) Fault-bounded horse with lateral ramps dipping in opposing directions on either margin. c) Overview of gently-curvilinear fold shown in Fig. 6a and ramps branching from the basal detachment. d) and e) are close-ups of the ramp shown in Fig. 7c that displays high-angle footwall cut-offs. (For interpretation of the references to colour in this figure legend, the reader is referred to the Web version of this article.)

and thrusts (Fig. 9a and b). AMS fabrics from within the gouge display sub-horizontal K_1 and K_2 clusters suggesting movement along the basal detachment towards the ESE-WNW (100–280°) (Fig. 9h). The angle between intermediate K_2 axes created around the LPS folds (Fig. 9c) and the LPS basal detachment (Fig. 9h) is 64°, and ~90° to the transport direction inferred from normals to folds and thrusts (Fig. 9b, g).

6.3. AMS fabrics created during LNS

6.3.1. AMS fabrics created during LNS shearing

We sampled a thin unit of gouge that is developed along the basal detachment immediately beneath the 'double vergence' fold geometries marking the LNS section (Fig. 8f and g, 10a, d, e). The AMS fabric of the gouge is characterized by a 'deformation fabric', with the K_1 and K_2 axes displaying well-defined sub-horizontal clusters (Fig. 10d). The trail of K_3

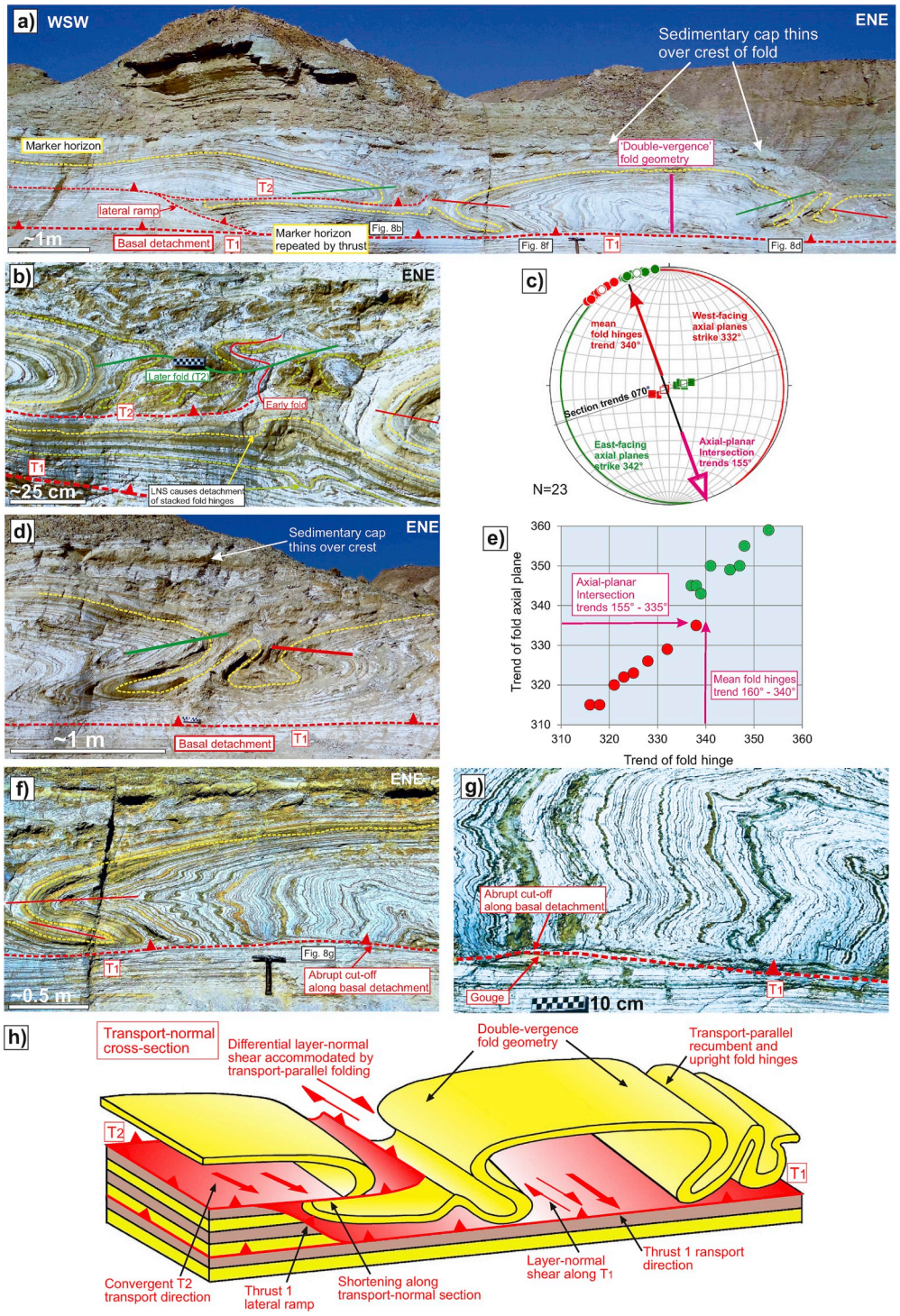

Fig. 8. a) View looking north at a WSW-ENE transport-normal section across thrusts and 'double vergence' folds deforming the same stratigraphic sequence and marker horizons (highlighted in yellow) as in the cutting exposed 100 m further NE (Fig. 4b and c). West-facing and east-dipping axial planes are highlighted in red, while east-facing and west-dipping axial planes are shown in green. b) Details of west-verging folds associated with Thrust 1 (T1) being refolded by east-verging folds linked to overlying Thrust 2 (T2). c) Stereonet showing the mean trend of fold hinges and mean strike of east facing and west-facing fold axial planes. Structural data on the stereonet is represented as follows: fold hinges (solid red/green circles), poles to east-facing fold axial planes (open green squares), mean pole to east-facing fold axial plane (solid green squares), poles to west-facing fold axial planes (open red squares), mean pole to west-facing fold axial plane (solid red squares), Calculated slump transport direction based on the axial-planar intersection method (AIM) is towards 155° (purple arrow) and is normal to the trend of the 070° outcrop section. d) Details of upright folding developed above Thrust 1 at the eastern-end of the outcrop. e) Graph that shows trends of south and west verging fold hinges and axial planes (in red) and south and east verging fold hinges and axial planes (in green). The trend of the reversal in fold vergence at ~340°–160° marks the approximate trend of transport. f) Detail of the western fold closure shown in d), with recumbent folds detaching on the underlying Thrust 1, creating high-angle cut-offs and gouge horizons shown in g). h) Summary cartoon highlighting structures formed in the transport-normal section shown in a). The older, underlying thrust (T1) is cut by the overlying thrust (T2), with lateral ramps marked by transport-parallel folding associated with differential LNS. The hammer (25 cm long with 20 cm head) and chequered rule (10 cm long) act as scales in the photographs. (For interpretation of the references to colour in this figure legend, the reader is referred to the Web version of this article.)

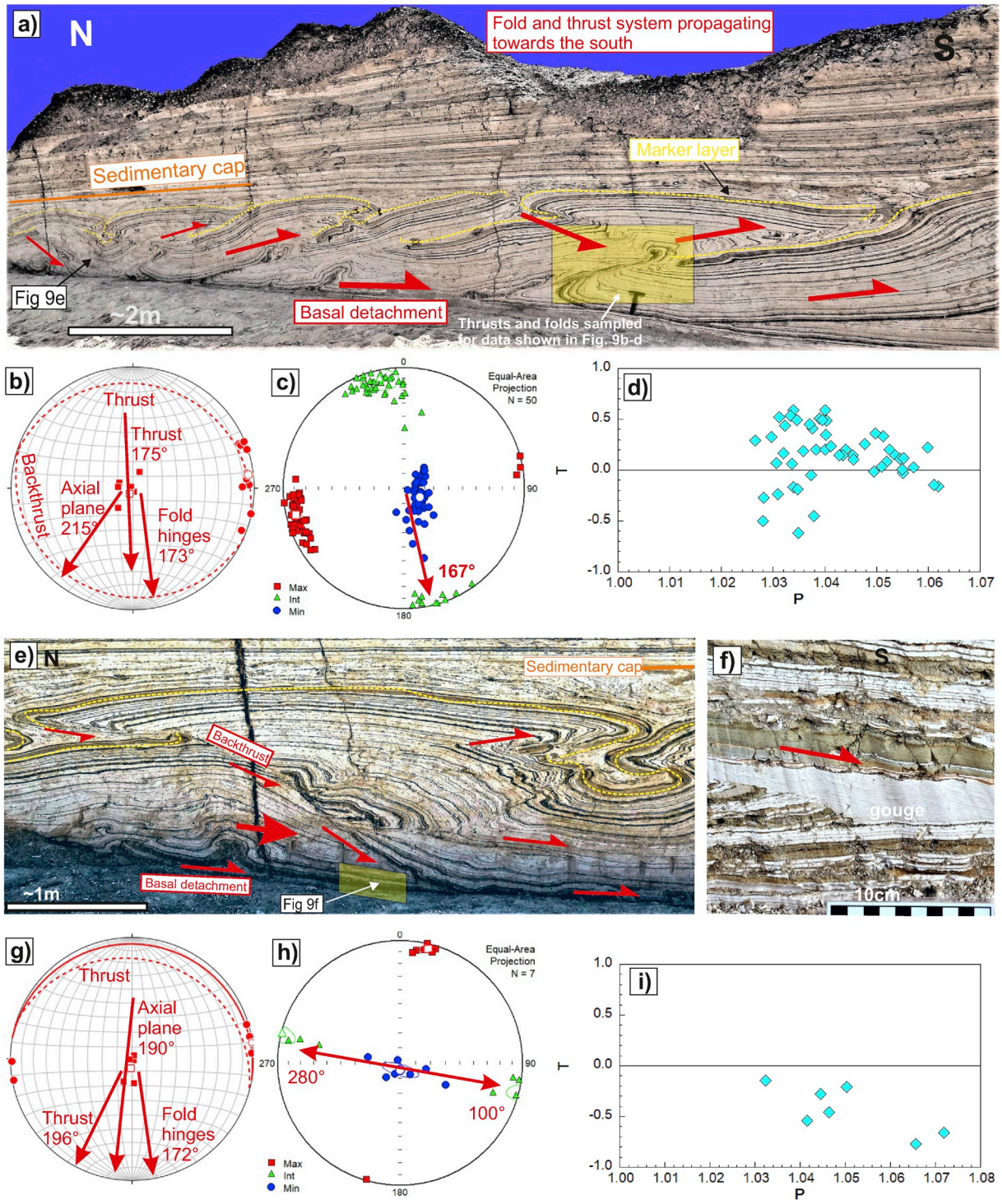

Fig. 9. a–i) Photographs, stereonets and associated AMS structural data from the transport-parallel cutting in the eastern LPS flow lobe (see Fig. 4a). a) General photograph of south-directed fold and thrust system. b) Stereonet showing orientations of thrusts, backthrusts fold hinges and poles to axial planes. The arrows represent transport directions based on normals to thrust strike, axial-planar strike and fold hinges. C) Lower hemisphere, equal-area projection stereoplots of AMS principal axes with 95% confidence ellipses, and d) *T-P* plot from folds in the LPS domain shown in a) and corresponding to structural data shown in b). e) Photograph of south-directed thrusts with backthrusts (location shown in a) f) Close-up photograph of fault gouge formed along the basal detachment that was sampled for AMS fabrics (location shown in Fig.9e). g) Stereonet showing orientations of thrusts, fold hinges and poles to axial planes. The arrows represent transport directions based on normals to thrust strike, axial-planar strike and fold hinges. h) AMS data from the gouge zone shown in f) and corresponding to structural data shown in g). i) Plot of AMS fabrics represented by *T* and *P* parameters. In AMS stereonets (c, h), maximum (K_1) axes are shown by red squares, intermediate (K_2) axes by green triangles and minimum (K_3) axes by blue circles. Trails of minimum K_3 axes (blue circles) are interpreted by red arrows. (For interpretation of the references to colour in this figure legend, the reader is referred to the Web version of this article.)

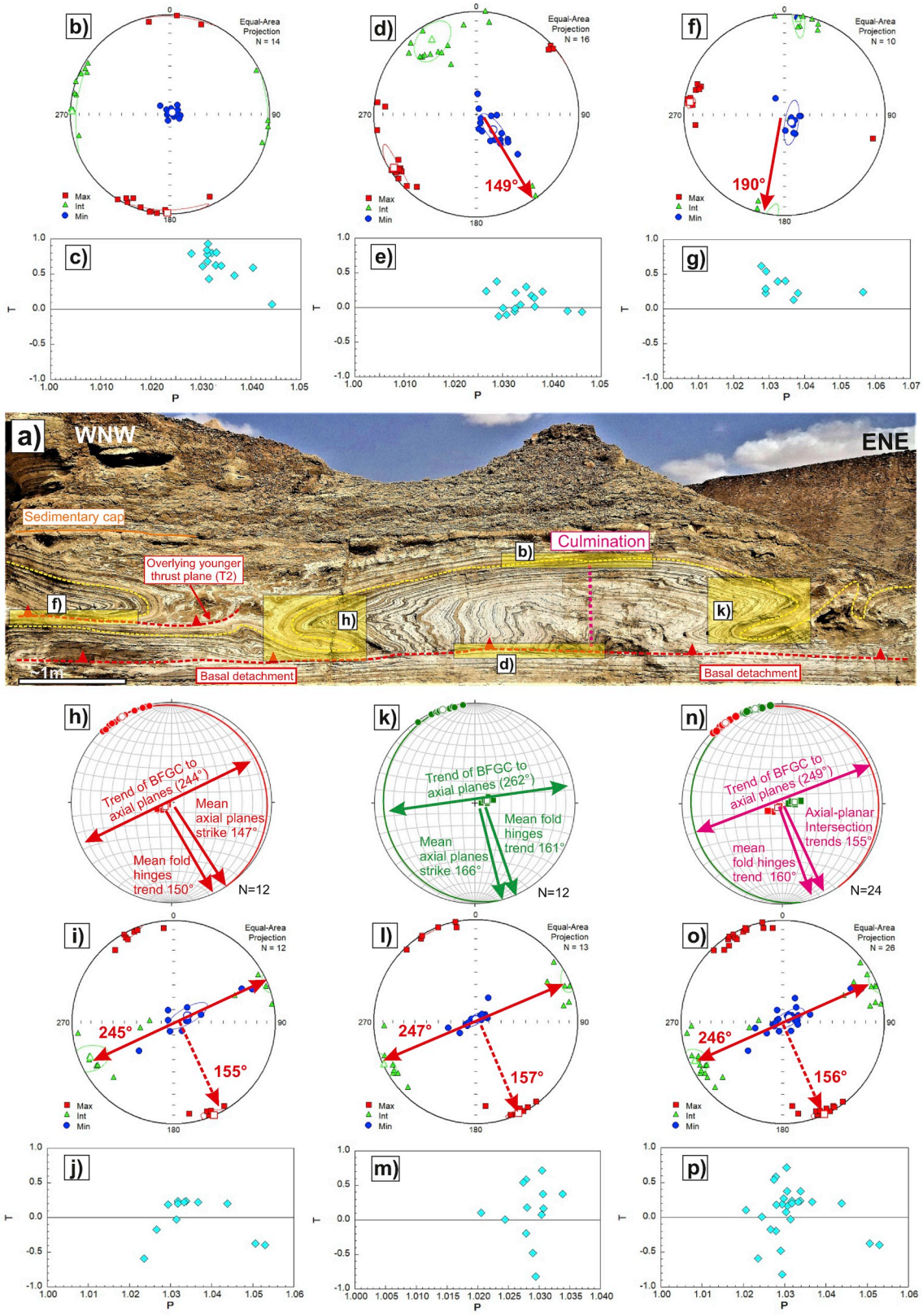

Fig. 10. a–e) Photographs, stereonets and associated AMS structural data from the transport-normal section in the central LNS-dominated zone (see Fig. 4a, j; 8a). a) General photograph showing location of samples and data. Stereoplots of AMS principal axes and *T-P* plots from b, c) the upper fold limb, d, e) the basal detachment, f, g) secondary overlying thrust plane (T2). Structural data, AMS fabric stereonets and T-P plots have been analysed from h, i, j) the WSW-verging fold closure; k, l, m) the ENE-verging fold closure; n, o, p) the combined WSW- and ENE-verging data shown in h-m). On structural stereonets (h, k, n), the trend of the best fit great circle (BFGC) has been drawn through poles to axial planes, otherwise all symbols used in stereonets and AMS plots are as described in Fig. 9.

axes suggests movement along the basal detachment towards the SSE (149°) (Fig. 10d). This is sub-parallel to the suggested movement direction (155°) from structural analysis of fold axial planes based on the Axial-planar Intersection Method (Alsop and Marco, 2012a) (Fig. 8c). We have also undertaken AMS analysis along detachments within the fold and thrust system ('T2' in Figs. 8b and 10a). AMS suggests movement is towards 190° (Fig. 10f) and therefore broadly consistent but oblique (~40°) with transport directions along the basal detachment. Discrepancies along the younger 'T2' may reflect flow around the culmination, or the effect of underlying lateral ramps (Fig. 8h).

6.3.2. AMS fabrics created during LNS folding

We have undertaken AMS fabric analysis around the previously described 'double vergence' folds created during LNS (Fig. 8a–h, 10a, 10 h-p). In this case, the K_1 axes and fold hinges broadly coincide with one another, while the K_3 and poles to axial planes also match (compare Fig. 10h with 10i, and 10 k with 10 l). The deviation of K_3 axes from verticality, forms a trend along 066°–246° and this is orthogonal to the direction of K_1 axes that correlate with mean fold hinges trending 340°–160° (compare Fig. 10n with 10°). The K_1 and K_2 axes have 'switched' by 90° between samples from the basal detachment and overlying fold hinges (compare Fig. 10d and o), while the angle between K_2 axes of Figs. 10d and o is 79°.

6.4. AMS parameters

The MTD in the case study was associated with an inelastic deformation during folding, as demonstrated by moderate to high values of P and L parameters and low T values (Figs. 9, 10, 11) and the linear correlation curve in T-L plot (Fig. 11).

This deformation is expressed by the formation of a magnetic lineation and a decrease in oblateness, as identified by the negative linear correlation curve (Fig. 11). In the T-L plot, the folds have high L values (up to 1.03) and low T values (up to −0.4) indicating that the strain magnitude of the folds was high (Levi et al., 2014) (Fig. 11). The L and T values of different structures created during LPS and LNS within the MTD are located in the middle or at the extreme end of the T-L curve (Fig. 11). This indicates that the deformation along the folded and sheared layers is heterogeneous (e.g., Weinberger et al., 2017). In addition, as the linear correlation curve is high, it means that the MTDs shared a somewhat similar degree of AMS anisotropy (P). Notably, the AMS parameters of the LPS detachments are unusual in that the lineation is very high ($L = 1.037$; Fig. 11; Table 1) and the shape of anisotropy

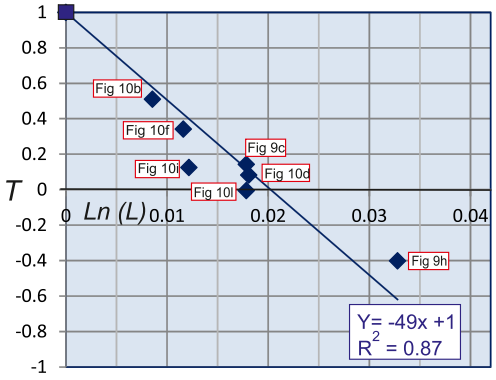

Fig. 11. T–L plot of gravity-driven mass transport deposits (MTDs). The solid blue line marks the linear correlation curve, with the labels next to blue diamonds indicating where data was collected. Filled blue square marks hypothetic sedimentation fabric where $T = 1$, $L = 1$ (Levi et al., 2018). Oblate fabrics are represented by $T > 0$, whereas $T < 0$ indicates prolate fabrics. (For interpretation of the references to colour in this figure legend, the reader is referred to the Web version of this article.)

is very prolate ($T = -0.44$; Fig. 9i; Table 1) when compared to parameters developed around the folds (Fig. 9d). This may suggest that there was a component of flow along the basal detachment that is parallel to the intersection of the adjacent thrust ramps (see discussion section 8.4).

7. Extension coeval with thrusting

Existing models of slope failure associated with MTDs suggest that extension associated with downslope-directed normal faults and shears should be concentrated towards the upslope head of the slump (e.g. Farrell, 1984; Farrell and Eaton, 1987) (Fig. 1). More recent models suggest that extension may locally develop anywhere within the slumped mass and may be linked to smaller second order flow cells that form during variable rates of translation within the MTD (Alsop and Marco, 2014). Within the case study, extensional faults are developed within the same MTD as the previously described contractional fold and thrust system (Figs. 12 and 13). They appear better developed in domains dominated by LPS, perhaps because pre-existing thrusts and folds are more suitably orientated for extension. Extensional faults typically display < 1 m displacement and are observed in both the west and east flow 'lobes' where shortening (and presumably thickening) has been greatest. In all cases the sedimentary cap that is deposited out of suspension following the failure event, is thickened in the hangingwall of normal faults, indicating that extension pre-dates or is synchronous with deposition of the cap.

7.1. Extension controlled by regional palaeoslopes

Within the case study, examples of extensional faults and shears that move towards the south down the regional palaeoslope are developed in both the eastern (Fig. 12a–d) and western flow lobes that are dominated by LPS (Fig. 12 e-g). Low-angle extensional faults cut across earlier folds and displace the hangingwall towards the south or south east (Fig. 12a and b). Refolding of marker layers is associated with rapid variations in displacement along the extensional faults, with displacement reducing towards a 'soft' downslope buttress (Fig. 12a–d). Downslope-directed extension also takes the form of more diffuse shearing and boudinage within tilted stratigraphy above thrust ramps near the yellow marker horizon (Fig. 12e–g). Boudinage of detrital-rich layers (see Ogata et al., 2014 for use of this terminology in MTDs) indicates that they are more competent than the surrounding aragonite-rich units, with extensional structures cutting and therefore post-dating the thrust-ramp related tilting. Collectively, these observations are consistent with downslope-directed extension that post-dates contractional folding and thrusting and is controlled by the regional palaeoslope towards the south.

7.2. Extension controlled by thrust topography

Although models of slope failure typically show extensional faults dipping in the downslope direction, it is possible for extensional faults to also dip upslope (see Alsop and Marco, 2011). In addition, extension may be controlled locally by the topography created by contractional structures, resulting in folds and faults verging away from underlying culminations (Alsop and Marco, 2011). We now describe examples of extensional faults from the case study, where movement is directed back up the regional slope ultimately leading to extensional reactivation of original thrust ramps.

7.2.1. Extensional faults steeper than thrusts

Extensional faults that are steeper than thrust faults lead to clear cross-cutting relationships (Fig. 13a–c). Extensional faults markedly cross cut folds and thrusts associated with SW-directed movement (Fig. 13d), with the hangingwall being displaced back up the regional palaeoslope (i.e. towards the north). The hangingwall of the extensional fault is commonly marked by a thickened sedimentary cap that is

Table 1
AMS data collected from samples in this case study. Notes: *N*, number of specimens; k_m, mean susceptibility (in 10^{-6} SI units); *L*, lineation; *P*, anisotropy degree; *T*, shape ellipsoid; *D*, *I* of K_i, declination and inclination of the susceptibility axis ($i = 1,2,3$).

Site	N	K_m (STD)	*L* (STD)	*F* (STD)	*P* (STD)	*T* (STD)	*D, I of* K_1 (Half confidence angles)	*D, I of* K_2 (Half confidence angles)	*D, I of* K_3 (Half confidence angles)
Fold-thrust system LPS	50	21 (8)	1.018 (0.007)	1.024 (0.007)	1.042 (0.01)	0.15 (0.28)	256, 09 (09/05)	347, 08 (11/08)	120, 78 (10/04)
Detachment LPS	7	16 (6)	1.037 (0.016)	1.013 (0.004)	1.05 (0.014)	−0.44 (0.24)	014, 05 (05/03)	284, 01 (13/04)	180, 85 (13/04)
ENE hinge zone LNS	13	38 (13)	1.012 (0.006)	1.016 (0.007)	1.029 (0.003)	0.13 (0.43)	155, 02 (08/04)	255, 01 (11/07)	360, 88 (11/04)
Top 'double-vergence' fold LNS	14	47 (13)	1.006 (0.005)	1.027 (0.003)	1.034 (0.004)	0.51 (0.22)	181, 02 (24/04)	272, 02 (25/04)	055, 88 (06/04)
WNW hinge zone LNS	12	28 (10)	1.018 (0.009)	1.017 (0.006)	1.035 (0.009)	−0.005 (0.30)	157, 01 (09/05)	247, 12 (19/08)	64, 78 (19/06)
T1 Detachment LNS	16	22 (6)	1.016 (0.004)	1.018 (0.003)	1.034 (0.005)	0.08 (0.16)	237, 05 (15/06)	329, 17 (17/12)	132, 72 (16/06)
T2 Detachment LNS	10	35 (5)	1.012 (0.005)	1.023 (0.005)	1.035 (0.009)	0.34 (0.16)	279, 08 (11/06)	10, 04 (12/07)	127, 81 (09/06)

STD - standard deviation and half confidence angles are in parentheses (Jelinek's statistics).

preserved in the down faulted area, while the 'yellow' marker horizon is below 'regional' elevation (Fig. 13a and b). In addition, thrusts within the immediate hangingwall of the extensional fault dip towards the south suggesting that they have been tilted and 'back-rotated' as extension and rotation occurred down the presumably listric normal fault (Fig. 13a, b, c). In some cases, the sedimentary cap infills tensile fractures that form adjacent to normal faults (Fig. 13b), indicating that extension occurred pre or syn deposition of the cap and is therefore broadly synchronous with MTD movement. This outcrop therefore forms an example of extension that cross cuts and immediately post-dates folding in an overall LPS setting.

7.2.2. Extensional faults parallel to thrusts

Extensional faults may form sub-parallel to adjacent thrusts, with their presence only being verified where the low-angle fault cuts distinct units such as the 'yellow' marker horizon (Fig. 13e). In detail, extensional faults in Fig. 13f and g cut the underlying and slightly steeper T2 thrust plane indicating that the extension immediately post-dates this (T2) thrust. However, the extensional fault is cut by the overlying thrust (T3) and extension therefore forms part of an overstep sequence with transport directed towards the south (Fig. 13h). The overlying (younger) T3 thrust depresses the underlying (yellow) marker indicating that extension had already occurred prior to the younger thrust that forms an overall overstep sequence (see Alsop et al., 2018) (Fig. 13e). Irrespective of the detailed timing relationships noted above, extension forms during the overall slump event and is 'sealed' by the overlying sedimentary cap. This outcrop therefore forms an example of extension that is broadly coeval with overall LPS.

7.2.3. Extension directly reactivates thrusts

In some cases, thrusts (with associated hangingwall anticlines) are reactivated resulting in a net extensional offset of marker beds (Fig. 13i and j). Extensional reactivation of existing thrusts results in the creation of new synforms above the extensional fault, meaning that both footwall synforms (developed during thrusting) and hangingwall synforms (created during extension) are found on each side of the reactivated fault (Fig. 13j and k). Measured fold hinges around such reactivated thrusts display a more scattered pattern than is typical, although the orientation of axial planes remains more consistent, with a pole 'trail' extending towards 134° and an overall average transport towards 162° (e.g. Fig. 13l). The 'back-collapse' down the existing thrust ramp occurs to a position that directly overlies the branching point of the underlying thrust ramp from the basal detachment, and suggests that the relative steepness of the underlying ramp may have partially controlled the extension (Fig. 13i). The thickened sedimentary cap in the hangingwall of the reactivated thrust demonstrates that extension is coeval with MTD movement.

8. Discussion

8.1. What fold patterns are created during layer-parallel and layer-normal shear in MTDs?

It is widely recognised that displacement gradients vary markedly in thrusts cutting unlithified sequences, with pronounced gradients both up the thrust plane and also potentially along the strike of the thrust (e.g. Totake et al., 2018). The implication is that MTDs may be expected to contain significant zones of LNS that accommodate such variations in displacement (e.g. Steventon et al., 2019). Although many seismic sections across MTDs are performed in a downslope direction parallel to overall transport, those sections that are transport-normal display variably-oriented thrusts and folds with opposing axial planar dips consistent with LNS (e.g. Fig. 13b in Armandita et al., 2015, Fig. 9 in Scarselli et al., 2016). Farrell and Eaton (1987) originally suggested that steeply-plunging folds may form in steep shear zones that are parallel to the downslope direction and accommodate differential (LNS) movement of the MTD. These authors proposed that differential downslope movement is linked to friction along the basal detachment that may reflect variations in pore fluid pressure.

Within the Zin case study, the 'central' LNS-dominated setting is marked by transport-parallel hinges rather than discrete strike-slip faults, while the LPS setting is dominated by gently arcuate folds and thrusts that form at high angles to transport (Fig. 4). Transport-normal sections (Fig. 8a) display transport-parallel cylindrical fold hinges together with axial planes that define double-vergence geometries indicating that components of LNS are developed (Alsop and Marco, 2012a). This is especially the case where lateral ramps are formed within the overstep sequence (Fig. 8h) (Coward and Potts, 1983; Alsop and Holdsworth, 1993, 2007; Debacker et al., 2009 Sharman et al., 2015). With increasing progressive deformation, transport-sub-parallel LNS folds are stretched and become highly-cylindrical (Alsop and Holdsworth, 2007). Little hinge rotation will occur as fold hinges are already sub-parallel to flow, and large amounts of strain are required to fully rotate hinges into complete parallelism with the shear direction (e.g. Escher and Watterson, 1974). The secondary thrusts on each side of the double-vergence folds reflect modest shortening created by the western and eastern flow cells moving slightly obliquely and converging towards one another (Fig. 8a, b, d, h).

In general, LNS is marked by high-angle hangingwall cut-offs, where steeply-dipping beds are abruptly truncated by the underlying basal detachment (Fig. 8f and g). The variable rotation and dip of fold axial planes during progressive shear in LPS-dominated settings results in

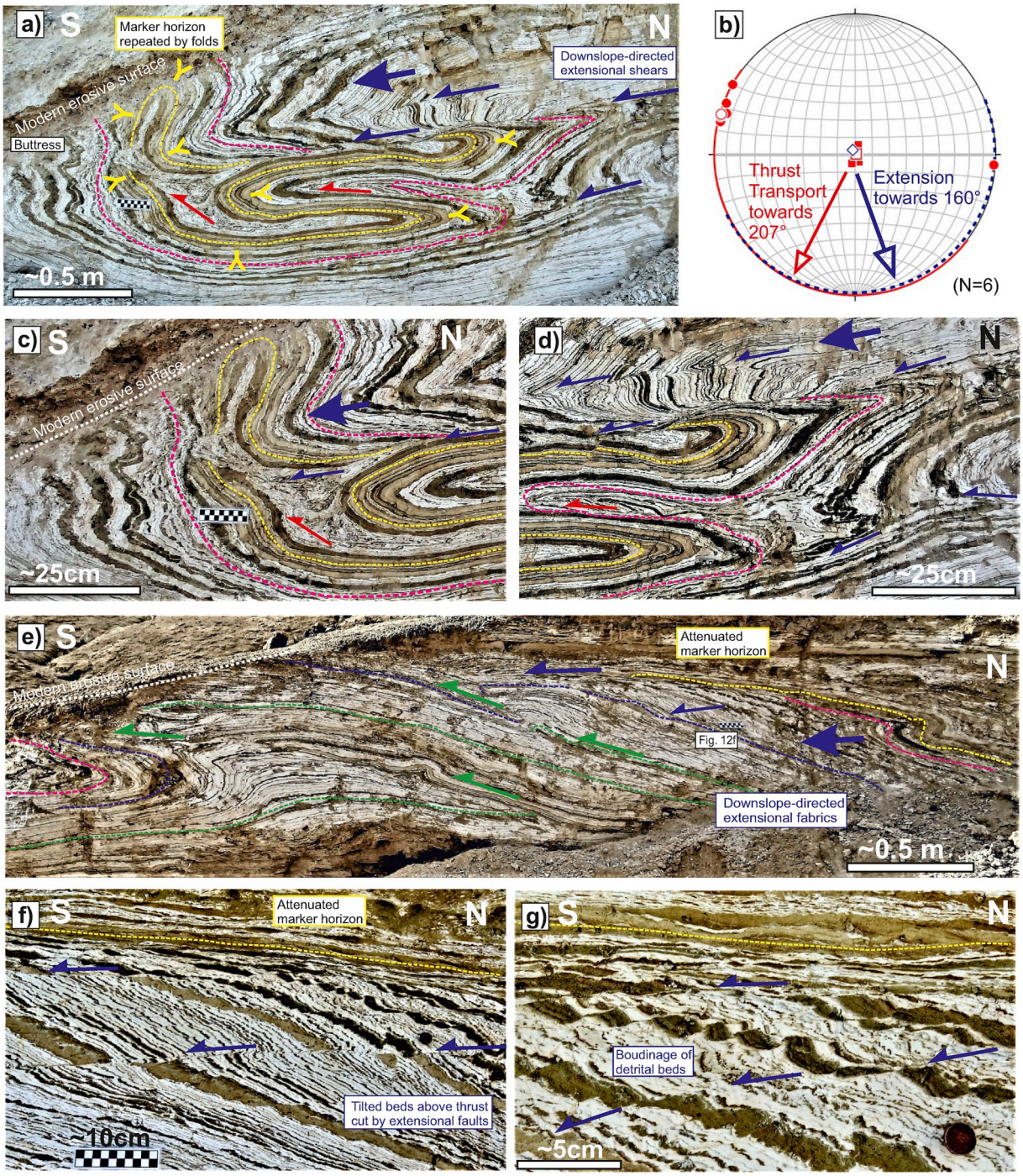

Fig. 12. Photographs and stereonets of folds and thrusts reworked by downslope-directed extensional faults and shears in a-d) the eastern flow lobe and e-g) the western flow lobe (see Fig. 4a). The distinctive 10 cm thick detrital marker horizon (highlighted in yellow) is folded and cut by extensional faults in a, c, d). The stereonet (b) shows fold hinges (solid red circles), mean fold hinge (open red circle), poles to fold axial planes (solid red squares), mean fold axial planes shown as a pole (open red square). Extensional fault data are shown in blue, with poles to faults (diamonds), pole to mean extensional fault (open diamond), mean extensional fault (dashed great circles). Calculated slump transport directions are based on combined fold hinge, axial plane and thrust data (red arrow) while mean extensional fault directions are shown by the blue arrow. e, f, g) show extensional shears and boudinage cutting a tilted sequence in the hangingwall of a thrust ramp. (For interpretation of the references to colour in this figure legend, the reader is referred to the Web version of this article.)

poles to axial planes forming 'trails' on stereonets that are parallel to the movement direction (e.g. Fig. 4f, h, i). Trails of axial-planar poles in LNS settings are much less well developed, with a clustering of poles more typical (Fig. 8c).

8.2. How does transport direction vary in different flow lobes within an MTD?

It has long been recognised that analysis of flow directions using the orientation of fold hinges and axial planes may be complicated by: a) the ability of folds to rotate towards the flow direction during progressive deformation; b) the ability of folds to be generated at different angles to

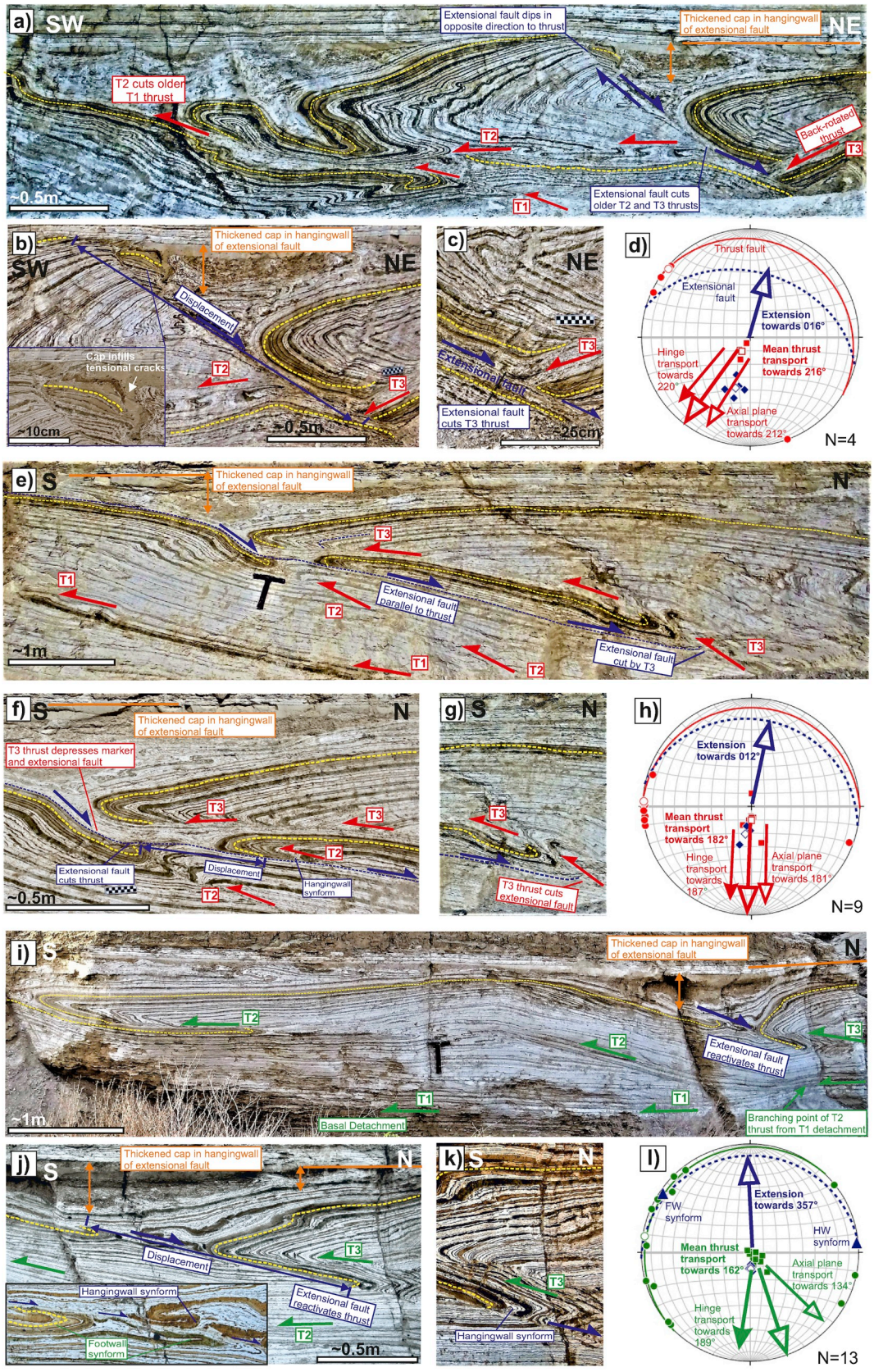

(caption on next page)

Fig. 13. Photographs and stereonets of folds and thrusts that cut the distinctive 10 cm thick detrital marker horizon (highlighted in yellow) and are then reworked by upslope-dipping extensional faults and shears. The sedimentary cap is thickened above the extensional fault in each case. a-c) Extensional fault dipping more steeply than thrusts, with associated structural data shown in stereonet (d). e-g) Extensional fault (marked by blue dashed line) dipping parallel to thrusts, with associated structural data shown in stereonet (h). Overlying thrusts cut the extensional fault in g). i-k) Extensional fault reactivating a thrust, with associated structural data shown in stereonet (l). Thrust numbering (T1, T2 etc.) refers to the local order of thrust development on each photograph and is not a universal scheme. Structural data on the stereonets (d, h, l) are represented as follows: fold hinges (solid red/green circles), mean fold hinge (open red/green circle), poles to fold axial planes (solid red/green squares), mean fold axial planes shown as a red/green great circle and the associated pole as an open red/green square. Extensional fault data are shown in blue, with poles to faults (diamonds), pole to mean extensional fault (open diamond), mean extensional fault (dashed great circles). In l), footwall (Fw) and hangingwall (Hw) synform hinges are shown by blue triangles. Calculated slump transport directions are based on combined fold hinge, axial plane and thrust data (red and green arrows), while mean extensional fault directions are shown by blue arrows. (For interpretation of the references to colour in this figure legend, the reader is referred to the Web version of this article.)

the transport direction during LNS; c) the ability of flow lobes within MTDs to contain different transport directions that define radial 'spreading' directions; d) combinations of the above (e.g. Coward and Potts, 1983). The overall flow pattern in the case study is summarised in Fig. 14a, while Fig. 14b provides a summary cartoon of the relationships.

8.2.1. *Folds rotate towards a constant flow direction*

Progressive deformation is generally considered to lead to rotation of fold hinges and their associated axial planes towards the flow direction and flow plane respectively (Escher and Watterson, 1974). This may ultimately lead to the development of highly-curvilinear sheath folds that arc around the flow direction (e.g. Alsop and Holdsworth, 2012). Within sub-horizontal simple shear-dominated systems, this will lead to large variations in fold hinge trends as folds tighten and rotate, whereas the strike of associated axial planes will not change significantly (Alsop and Carreras, 2007).

Within the Zin case study, there is no notable increase in fold tightness as hinge trends rotate towards the central zone (Fig. 4a). For instance, the geometries of ~E-W trending folds in the transport-parallel cutting (Fig. 5a–d) are almost indistinguishable from the NNW-trending hinges that affect the same stratigraphy ~100 m further west near the central zone (Fig. 5e and f). In addition, the strike of axial planes also varies significantly (>45°) towards the central zone (e.g. compare Fig. 5b, d with Fig. 5 f), which is the opposite to that expected within sheath folds where axial planar trends remain fairly

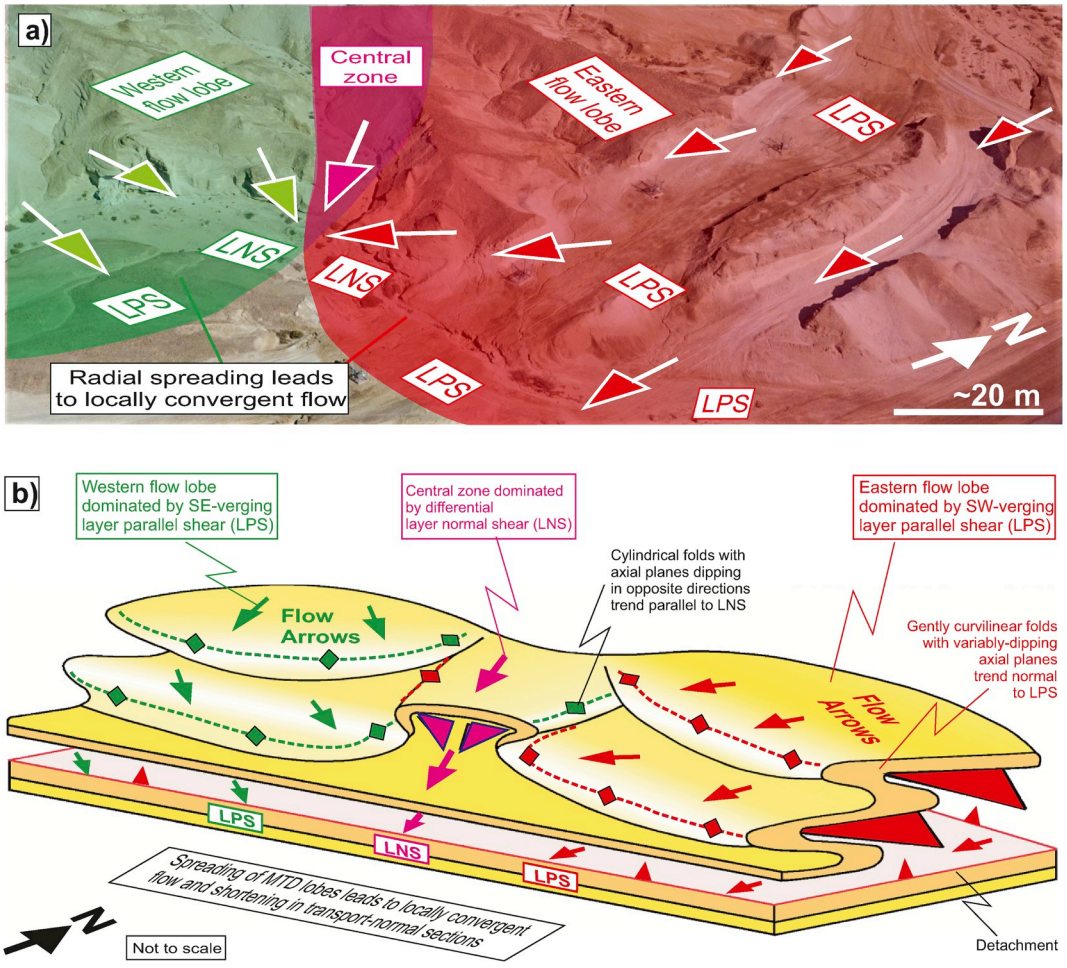

Fig. 14. a) Interpreted western (green) and eastern (red) flow lobes separated by a central zone (purple) superimposed on an oblique aerial photograph of the case study. b) Schematic summary cartoon of the case study MTD. Western and eastern flow lobes developed during layer parallel shear (LPS) are separated by a central zone dominated by layer normal shear (LNS). Flow arrows display slight radial patterns within each lobe resulting in broadly convergent transport, with gently-curvilinear folds developed at high angles to LPS flow, whereas transport-parallel 'double-vergence' folds mark differential LNS. (For interpretation of the references to colour in this figure legend, the reader is referred to the Web version of this article.)

constant. Within the central zone, variably trending fold hinges display a concomitant variation in axial planar strike (e.g. Fig. 8e) that does not support a 'fold rotation model'. We therefore suggest that the large-scale variation in fold patterns observed within the flow lobes are not a consequence of sheath folding associated with progressive deformation.

8.2.2. Folds initiate at different angles to a constant flow direction

Traditional models of flow cells suggest that the transport direction remains relatively constant, while folds and shears may systematically vary about this direction due to the addition of variable components of LNS (e.g. Coward and Potts, 1983; Alsop and Holdsworth, 1993). LNS associated with differential dextral shear results in 'S' fold hinges trending anticlockwise of flow, but clockwise of the associated axial planar strike. Conversely, sinistral shear is marked by 'Z' fold hinges trending clockwise of flow but anticlockwise of the associated axial planar strike (Alsop and Holdsworth, 2007) (Fig. 2b). As folds initiate in different orientations, there is no requirement for folds developed sub-parallel to flow to have necessarily rotated into that orientation with associated tightening of fold hinges.

Within the Zin case study, the western flow lobe is marked by fold hinges generally trending anticlockwise of their associated axial planes that strike NE-SW (Fig. 4a, c, k, 6a-d), whereas the flank of the eastern flow lobe is marked by fold hinges generally trending clockwise of their associated axial planes that strike NW-SE (e.g. Fig. 4a, d, i). This is consistent with sinistral shear in the lateral margin of the western lobe and dextral LNS in the eastern lobe, and suggests that the lateral margins of each lobe have 'lagged' behind the middle of the lobes that flowed more rapidly. The detailed fold and fabric patterns therefore support a model of differential LNS around the lateral margins of each flow lobe.

8.2.3. Folds form around variable transport directions marking flow lobes

Farrell (1984) recognised that the bulk (downslope) transport direction of MTDs may be relatively constant and oblique to the lateral propagation of underlying failure surfaces. However, within MTDs it has also been recognised that flow directions may vary from an outcrop scale (e.g. Strachan and Alsop, 2006) to a larger seismic scale (e.g. Armandita et al., 2015) in a similar manner to that modelled around spreading orogenic nappes (e.g. see Fossen, 2016, p.371). Strachan and Alsop (2006, p.465) suggested that constant flow directions should not be automatically assumed as a change in fold orientation without a corresponding variation in fold style may reflect lateral or 'radial' spreading within 'lobes' at the toe region of the MTD (e.g. see Fossen, 2016, p. 388). Radial spreading would lead to extension at high angles to flow, resulting in conjugate normal fault systems trending broadly parallel to MTD flow as described elsewhere in the Lisan Formation by Alsop and Marco (2011). Extensional movement that converges from different directions has been invoked by Armandita et al. (2015, p. 391) to create a range of downslope compressional structures (folds, thrusts) and strike slip faults in a seismic scale example of mass transport from offshore Borneo.

Within the Zin case study, a component of fold and thrust-related shortening along the transport-normal section indicates a degree of convergent flow during slumping (Figs. 4a and 8h). In detail, the western flow lobe is marked by NE-SW trending folds that are gently-curvilinear about the calculated SE-directed flow direction (Fig. 6a–d). During LNS, fold hinges are typically cylindrical and do not display such curvilinear hinges, and we therefore invoke a component of SE-directed radial flow in the western lobe. In the eastern lobe, the calculated fold transport –direction at the southern end of the transport-parallel section (Fig. 4a and b) is slightly (13°) SW (clockwise) of the thrust transport-direction, and also suggests that there may have been a component of 'radial spreading' and convergent flow towards the SW at the downslope toe of the slump (e.g. Strachan and Alsop, 2006). In summary, we suggest that complex flow patterns are created by combinations of LPS and LNS (see section 8.2.2. above). In addition, the flow direction may also locally vary, with SE-directed flow in the western lobe and SW-directed flow in the eastern lobe, reflecting radial spreading of second-order flow lobes in the toe of the MTD, as summarised in Fig. 14a and b.

8.3. How do thrust systems interact with one another in MTDs?

Butler (1982, p.239) noted that orogenic thrust systems may form by either of two 'end member' propagation models termed 'piggyback' (e.g. Dahlstrom, 1970, p. 349) where propagation is directed towards the orogenic foreland, or 'overstep' where propagation is in the opposite direction to the thrust transport direction. In addition, it has become increasingly apparent that more than one thrust may move at the same time, to create 'synchronous thrusting' (e.g. Boyer, 1992; Butler, 2004; Alsop et al., 2018). In gravity-driven fold and thrust systems that form MTDs, 'piggyback' systems equate to propagation down the regional slope, whereas 'overstep' systems reflect propagation back up the regional slope.

Within the case study, individual thrust systems dominated by LPS may be modelled in terms of localised flow cells that translate downslope in an overall overstep thrust sequence that contains synchronous thrusting (Fig. 15a) (Alsop et al., 2018). Thrusts that are positioned downslope are considered to have formed first in an overstep sequence, and typically have larger offsets as they have had more time to accrue displacement during synchronous thrusting (Fig. 15b) (Alsop et al., 2018). As displacement increases, thrusts may propagate laterally to create linkages between adjacent segments at both the outcrop (e.g. Watkins et al., 2017) and seismic scales (e.g. Totake et al., 2018). In the case study, interaction between adjacent and simultaneous flow cells results in localised areas of differential sinistral and dextral LNS (Fig. 15a). Where variations in thrust rates between cells change only gradually, compatibility may be maintained by zones of oblique strain (e.g. Coward and Potts, 1983; Alsop and Holdsworth, 1993), which may create locally oblique folds and thrusts during synchronous thrusting. The overall slight radial 'spreading' of MTDs leads to locally convergent movement between adjacent flow lobes as observed in the transport-normal section (Figs. 1, 7, 14a, b, 15a). Where localised flow cells develop during translation of the MTD, systematic patterns of displacement will develop within each flow cell, with adjacent cells potentially displaying different amounts of displacement. Displacement profiles will therefore vary across strike suggesting that systematic patterns can only be measured within individual cells (Fig. 15b). In addition, as new overstep thrusts form further upslope, they may be influenced by earlier (downslope) structures that may create a pre-existing local bathymetry. Thrust-generated thickening leading to local bathymetry around flow lobes may therefore encourage radial spreading away from underlying structural highs in the overlying younger thrusts. Bathymetry may be reduced and become subdued due to extensional faults that form parallel to, or reactivate, existing thrusts (Fig. 15a). This may also result in flow directions (and associated AMS fabrics discussed below) varying locally around obstructions.

8.4. Can AMS fabrics be used to distinguish transport-parallel and transport-normal folds?

The AMS fabric from MTDs within the Lisan Formation is a classic 'deformation fabric' with clustered AMS axes and weak to prolate ellipsoid shape (Levi et al., 2006a, b, 2014, 2018; Jacoby et al., 2015; Weinberger et al., 2016, 2017). As MTDs within the Lisan Formation were not deformed by post-slumping tectonics, their fabric preserves that of the actual MTD 'event' (Weinberger et al., 2017). It has long been established that bedding-parallel shear during slumping would tend to physically rotate particles along horizontal axes in such a way that in a lower hemisphere projection, rotation would result in the particle short axes pointing toward the transport direction (Rees, 1966). Because the particle short and long axes coincide with the direction of the minimum and maximum susceptibility axes respectively, the magnetic fabrics of

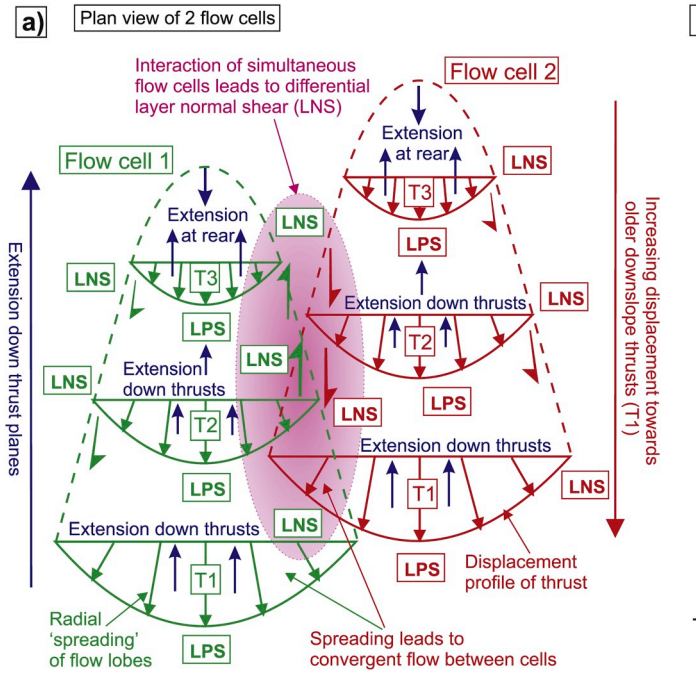

Fig. 15. Stylised diagram illustrating a) interaction of translating flow cells along a basal detachment within a MTD, and b) displacement-distance graphs across the flow cells shown in a). The shape and distribution of flow cells that form along the basal detachment is entirely schematic. Movement along each thrust (T1, T2 etc.) are shown by individual displacement profiles that define stylised gradients towards lateral terminations. The thrusts follow an overstep sequence of initiation (T1, T2 etc.) and then move synchronously downslope, such that older thrusts (T1) accrue the larger displacements. The green and red flow cells (labelled 1 and 2 respectively) are also considered to move simultaneously to create potential areas of layer-parallel shear (LPS) and differential layer-normal shear (LNS) between them. Subsequent extensional movement back down thrust planes is shown by blue arrows. See text for further detail. (For interpretation of the references to colour in this figure legend, the reader is referred to the Web version of this article.)

slumped sediments have trails of K_3 axes pointing toward the transport direction, and well-clustered K_1 axes parallel to fold hinges (Weinberger et al., 2017).

8.4.1. AMS-derived transport directions

Our structural analysis has demonstrated that the AMS fabrics forming during LPS are strongly related to the vergence of the fold-thrust systems and have the following relationships to the transport direction: (1) K_1 axes are parallel to the fold hinges and strikes of thrusts, and are oriented normal to the axis of the transport direction; (2) K_2 axes are oriented normal to the fold hinges and parallel to the axis of the transport direction; and (3) K_3 axes deviate from the vertical, showing a trail of axes directed toward the absolute transport direction.

Using the directional deviation of K_3 from verticality described above, the AMS fabrics taken from gouge zones marking the detachment horizons (T1 and T2 thrusts in Figs. 8 and 10d-g) in areas of differential LNS provide a first-order indication for the transport direction (compare Fig. 10 d with 10n). It seems that local deviations towards the SSE along T2 in the central zone (Fig. 10f) may reflect deflections around underlying and older thrust culminations.

The AMS-derived transport direction parallels the interpreted flow direction from axial planes and hinges. Likewise, we interpret the transport direction of the gouge zone directly beneath thrust ramps marking LPS. In this zone, the AMS fabric indicates that a component of strike-parallel flow evolved, potentially suggesting that such flow may develop along branch lines marking backthrust ramps. We speculate that such along-strike flow may be driven by fluid pressures, with the nearest lower pressure area actually towards the lateral margins of MTDs where stratigraphic thickness has not been markedly increased by thrusting and folding. As such, it may relate to very high lateral displacement gradients when thrusts are traced along strike (e.g. Totake et al., 2018). In summary, the AMS axes are clearly controlled by the orientation of the fold hinges and associated axial planes from where they were sampled. However, while AMS 'honours' the orientation of its host fold, it does not discriminate between different mechanisms of fold generation in LNS and LPS environments. Consequently, fold hinges that form oblique or sub-parallel to transport in LNS dominated settings may generate AMS fabrics that do not simply reflect the direction of bulk shearing.

8.4.2. Internal AMS fabrics

The depositional AMS fabric of the Lisan Formation is strongly oblate and is prone to changes during deformation (Levi et al., 2018). In the fold and thrust system developed during LPS, the fabric of the gouge zones along the ramps is typically oblate (Weinberger et al., 2017), but that below the ramp is strongly prolate and probably related to shearing during strike-parallel flow at that locality (Fig. 9e–i, 11). In hinge zones, both in LPS- and LNS-related folds, the fabrics show a tendency toward prolate and are much different from the oblate fabric detected at the top flat layer of the double vergence fold (Fig. 10a, b, c, 11). However, although the AMS fabrics are controlled by the folds, they do not differentiate how these folds were created in potential zones of either differential LNS or simple LPS. The basal detachments formed during LNS also show a tendency toward prolate AMS fabrics (Fig. 10d and e, 11), indicating that shearing played a major role during slumping along this plane.

8.5. Could extensional reactivation of thrusts conceal 'missing' contraction in MTDs?

Two models potentially explain either footwall or hangingwall movement along the extensional faults that have been recognised: a) lateral extrusion of the footwall block down the regional slope (Fig. 16a): b) collapse of the hangingwall block down the fault plane (Fig. 16b). Within the case study, lateral downslope extrusion of the footwall may be enhanced by the overstep thrust sequence, as younger thrusts forming above older structures will add to the loading experienced in the footwalls (Fig. 16a). This may also partially explain the AMS fabrics that suggest along-strike movement of sediment directly beneath thrust ramps (Fig. 9e–i). However, we do not believe that footwall extrusion forms a significant component of movement along the extensional faults as: a) detailed timing relationships show that extensional faults are cut by overlying thrusts i.e. extension pre-dates adjacent thrusts and is not a consequence of this additional thrust-generated loading (Fig. 13e–h); b) marker horizons are displaced to below regional levels in the hangingwall of the extensional faults (Fig. 13a,e,i); c) extensional reactivation of thrusts (and extensional faults parallel to thrusts) are typically formed where the sequence has been steepened along underlying thrust ramps (i.e. the hangingwall sequence was

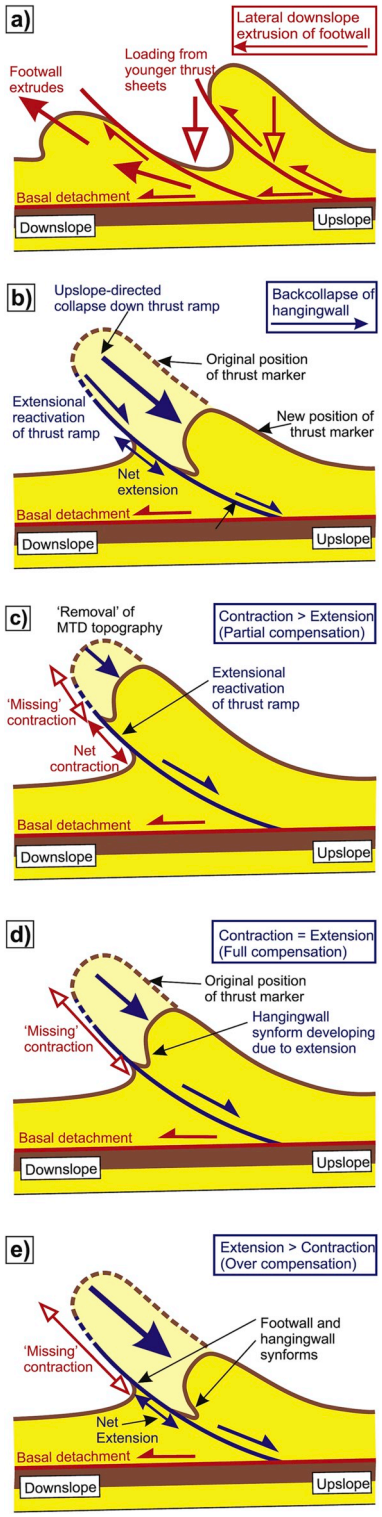

Fig. 16. a) 'Lateral extrusion model' where the footwall to the original thrust fault moves downslope due to the loading from younger overlying thrust sheets. b) 'Back collapse model' where the hangingwall to the thrust fault is reactivated and slips back down the original thrust ramp resulting in movement up the regional slope. The 'Back-collapse model' may result in c) extension only partially compensating for the original thrust displacement, d) extension fully compensating the original thrust displacement, and e) extension over-compensating for the original thrust displacement leading to net extension along the fault. In d) and e), the original contraction is now entirely 'missing' and the only evidence for reactivation may be the development of a hanging-wall synform above the extensionally reactivated thrust fault.

steeper and therefore potentially more unstable) (Fig. 13e, i); d) the sedimentary cap is thickened above the extensional fault suggesting the hangingwall has moved down to form accommodation space and resultant growth sequences in the cap (Fig. 13a,e,f,i,j); e) tensional fractures infilled by the sedimentary cap are developed in the hang-ingwall of the extensional fault, suggesting extension rather than continued contraction (Fig. 13b), f) thrusts that are reactivated as extensional faults maintain pristine fault angles, and have not been rotated to lower angles of dip as might be expected if the footwall block was extruded laterally (Fig. 13i). In fact, in the upslope dipping exten-sional faults (Fig. 13a), it is the hangingwall block that has been back rotated as it moves down the (presumably) listric normal fault plane. Collectively, these observations and inferences support 'collapse' and movement of the hangingwall block down the regional slope where extensional faults are observed to cut thrusts (Fig. 13), or back down the thrust plane (i.e. up the regional slope) where thrusts are reactivated (Fig. 13).

Having established the kinematics of normal faults, where the hangingwall blocks (with associated marker beds) 'drop' back down to the regional elevation, we note that no significant topography is pre-served on the top MTD surface prior to deposition of the overlying sedimentary cap (e.g. Alsop et al., 2018). This 'self-equilibration' results in a lack of topography on MTDs and has been previously noted by Frey-Martinez et al. (2005, 2006). In the Zin case study, folds and thrusts are directed towards either the SW (Fig. 13a–d), south (e.g. Fig. 13e–h) or SE (e.g. Fig. 13i-l) and are affected and potentially reactivated during extension. This suggests that extension and collapse is controlled by local MTD geometries linked to flow 'lobes' and/or topography, rather than the orientation of the overall palaeoslope that is unlikely to change over such short distances. In summary, extension is a consequence of the exceptionally weak nature of these sediments that are therefore unable to 'build' topography.

While we can only categorically recognise reactivation of thrusts where extension is greater than contraction (i.e. net extension is pre-served), it is likely that other thrusts may have been reactivated but extension has failed to fully compensate the earlier shortening (partial compensation) (Fig. 16c,d,e). In such cases, extension may only be suggested from the 'duel' synformal geometries above and below the thrust plane (Fig. 16d and e). Such 'duel' synforms on either margin of the fault are not simply a consequence of a later fault cutting across a pre-existing synform as it is the same marker layer (e.g. yellow marker on Fig. 13f, j) that defines the synform on both sides of the fault. While a later cross-cutting fault may repeat the along strike continuation of a fold, it cannot duplicate the same structure affecting the same strati-graphic level. Therefore, the synforms were created at different times during contraction (footwall synform) and later extensional collapse (hangingwall synform). Creation of folds in both the footwall and hangingwall of reactivated thrust faults is similar to structures formed during reactivation of normal faults during basin inversion (e.g. see Fossen, 2016, p.373).

A further implication of extensional reactivation of thrust ramps is that calculations of total displacement on distance-displacement (D-D) plots are likely to underestimate thrust movement that have been partially restored. This has obvious consequences for balancing and restoration of thrust sequences at both outcrop and potentially on seismic sections. Seismic-scale examples of collapse and extension along thrust imbricates in the compressional zone of MTDs is provided by Armandita et al. (2015). Furthermore, the shortening that is apparently missing from MTDs on many seismic sections (e.g. Butler and Paton, 2010; de Vera et al., 2010) may reflect the variable extensional overprint restoring and 'removing' some of the original contraction after each thrust displacement. Slippage back down thrust ramps reflects the in-fluence of gravity and the extremely weak nature of the sediments, potentially combined with enhanced fluid pressure along thrusts. It could be argued that steeper thrusts, or thrusts that are subsequently back-steepened, may undergo the most significant displacement linked

to collapse, although net (horizontal) extension and displacement may actually be less on these steeper faults due to their being less efficiently orientated to accommodate horizontal extension. Difficulties in balancing upslope extension with downslope contraction may be due to out-of-plane extensional movement (e.g. Alsop and Marco, 2011), out-of-plane contractional movement linked to radial spreading of MTDs, together with sub-seismic scale deformation that is not 'visible' on seismic (see Alsop et al., 2020c). The potential for extensional reactivation of thrusts described above provides a further mechanism to explain why contraction is apparently 'missing' from seismic sections across MTDs.

9. Conclusions

We have undertaken detailed structural analysis in both transport-parallel and transport-normal sections in order to investigate the 3D geometry of flow lobes developed within MTDs around the Dead Sea Basin. This allows us to draw the following general conclusions.

1) Within MTDs, LPS results in gently-curvilinear fold hinges that typically verge downslope and arc around the flow direction. During progressive downslope-directed shear axial planes may rotate towards the flow plane, resulting in trails of poles on stereographic projections that are aligned with the flow direction.
2) Variation in the amount and direction of downslope-directed movement results in LNS that is accommodated by lateral-ramps and recumbent to upright cylindrical fold hinges that are developed oblique or sub-parallel to flow. LNS is marked by 'double vergence' geometries where S and Z fold hinges and associated axial planes display systematic obliquity to the flow direction. The calculated intersection between Z and S axial planes is parallel to the flow direction. LNS also results in bedding displaying abrupt footwall cut-offs along detachments.
3) Flow lobes within the studied MTDs are developed over tens of metres and display up to 45° variation in the flow direction. They are associated with radial spreading that resulted in convergent flow between adjacent lobes. Folds developed sub-parallel to the bulk flow direction may be a result of this locally convergent flow, together with differential LNS.
4) Interaction of simultaneous flow cells during translation of the MTD potentially results in a range of overprinting and shear scenarios. Transport-normal sections reveal that overlying thrusts refold structures related to underlying thrusts, thereby supporting a broadly overstep sequence where deformation migrates upslope during retrogressive failure. Systematic variations in displacement recorded during synchronous thrusting can only be measured parallel to the transport direction within individual cells.
5) The AMS fabrics display systematic relationships around folds within MTDs of the Lisan Formation, with K_1 axes developed parallel to fold hinges and K_3 axes parallel to the poles of axial planes. The AMS fabrics formed during the folding reflect the local internal deformation within the folds. This does not mean that the AMS will always point to a direction of transport as the AMS does not differentiate how these folds were created in zones of either LPS or differential LNS. During LPS, fold hinges form normal to the flow and AMS fabrics therefore provide reliable indicators of the transport direction. During LNS, fold hinges form at variable angles to flow and AMS fabrics are therefore a less robust indicator of flow. Caution should be exercised when interpreting kinematics from AMS fabrics around folds alone, as folding may form at a variety of orientations relative to transport. Notably, AMS taken from gouge zones marking detachment horizons directly below areas of differential LNS provide a first-order indicator for the transport direction. It would appear that where AMS is taken from gouge zones directly beneath thrust ramps marking LPS, then there could be a component of strike-parallel flow marked by prolate fabrics.
6) Extension may directly reactivate existing thrusts, or create new extensional faults that are sub-parallel to thrusts or cut across them at steeper angles. The 'back-collapse' model is driven by local topography created by the thrusts. Extensional faults are overlain by the sedimentary cap and locally cause it to thicken, indicating that collapse is part of the same overall MTD. Extension may only partially compensate, fully compensate, or over compensate contraction resulting in net extension along the original thrust plane. Although limited extension may be difficult to recognise, it may cause synforms to develop in both the hangingwall and footwall of the original thrust planes. Extensional reactivation of thrusts may help explain why contraction is apparently 'missing' when attempts are made to 'balance' contraction and extension imaged on seismic sections across offshore MTDs.

Declaration of competing interest

We can confirm that there are no conflicts of interest with this work.

CRediT authorship contribution statement

G.I. Alsop: Conceptualization, Formal analysis, Writing - original draft. **R. Weinberger:** Conceptualization, Formal analysis, Writing - original draft. **S. Marco:** Conceptualization, Formal analysis, Writing - original draft. **T. Levi:** Conceptualization, Formal analysis, Writing - original draft.

Acknowledgements

RW was supported by the Israel Science Foundation (ISF grant No. 868/17). SM acknowledges the Israel Science Foundation (ISF grant No. 1645/19). TL was supported by a grant from the Israeli Government under Geological Survey of Israel DS project 40706. We thank Iyad Swaed for the drone photography, Stephen Laubach for editorial handling, and Jacub Fedorik and an anonymous reviewer for constructive comments.

References

Agnon, A., Migowski, C., Marco, S., 2006a. Intraclast breccia layers in laminated sequences: recorders of paleo-earthquakes. In: Enzel, Y., Agnon, A., Stein, M. (Eds.), New Frontiers in Dead Sea Paleoenvironmental Research. Geological Society of America Special Publication, pp. 195–214.
Agnon, A., Weinberger, R., Zak, I., Sneh, A., 2006b. Geological Map of Israel. Sheet 20-I, II Sedom, Scale 1:50,000. Israel Geological Survey, Jerusalem.
Alsop, G.I., Carreras, J., 2007. Structural evolution of sheath folds: a case study from Cap de Creus. J. Struct. Geol. 29, 1915–1930.
Alsop, G.I., Holdsworth, R.E., 1993. The distribution, geometry and kinematic significance of Caledonian buckle folds in the western Moine Nappe, northwestern Scotland. Geol. Mag. 130, 353–362.
Alsop, G.I., Holdsworth, R.E., 2007. Flow perturbation folding in shear zones. In: Ries, A. C., Butler, R.W.H., Graham, R.D. (Eds.), Deformation of the Continental Crust: the Legacy of Mike Coward, vol. 272. Geological Society, London, pp. 77–103. Special Publications.
Alsop, G.I., Holdsworth, R.E., 2012. The three dimensional shape and localisation of deformation within multilayer sheath folds. J. Struct. Geol. 44, 110–128.
Alsop, G.I., Marco, S., 2011. Soft-sediment deformation within seismogenic slumps of the Dead Sea basin. J. Struct. Geol. 33, 433–457.
Alsop, G.I., Marco, S., 2012a. A large-scale radial pattern of seismogenic slumping towards the Dead Sea Basin. J. Geol. Soc. 169, 99–110.
Alsop, G.I., Marco, S., 2012b. Tsunami and seiche-triggered deformation within offshore sediments. Sediment. Geol. 261, 90–107.
Alsop, G.I., Marco, S., 2013. Seismogenic slump folds formed by gravity-driven tectonics down a negligible subaqueous slope. Tectonophysics 605, 48–69.
Alsop, G.I., Marco, S., 2014. Fold and fabric relationships in temporally and spatially evolving slump systems: a multi-cell flow model. J. Struct. Geol. 63, 27–49.
Alsop, G.I., Marco, S., Levi, T., Weinberger, R., 2017a. Fold and thrust systems in mass transport deposits. J. Struct. Geol. 94, 98–115.
Alsop, G.I., Marco, S., Weinberger, R., Levi, T., 2016. Sedimentary and structural controls on seismogenic slumping within mass transport deposits from the Dead Sea basin. Sediment. Geol. 344, 71–90.
Alsop, G.I., Marco, S., Weinberger, R., Levi, T., 2017b. Upslope-verging back thrusts developed during downslope-directed slumping of mass transport deposits. J. Struct. Geol. 100, 45–61.

Alsop, G.I., Weinberger, R., Marco, S., 2018. Distinguishing thrust sequences in gravity-driven fold and thrust belts. J. Struct. Geol. 109, 99–119.
Alsop, G.I., Weinberger, R., Marco, S., Levi, T., 2019. Identifying soft-sediment deformation in rocks. J. Struct. Geol. 125, 248–255. https://doi.org/10.1016/j.jsg.2017.09.001.
Alsop, G.I., Weinberger, R., Marco, S., Levi, T., 2020a. Bed-parallel slip: identifying missing displacement in mass transport deposits. J. Struct. Geol. 131, 103952.
Alsop, G.I., Weinberger, R., Marco, S., Levi, T., 2020b. Folding during soft-sediment deformation. In: Bond, C.E., Lebit, H.D. (Eds.), Folding and Fracturing of Rocks: 50 Years since the Seminal Text Book of J.G. Ramsay, vol. 487. Geological Society Special Publication, pp. 81–104. https://doi.org/10.1144/SP487.1.
Alsop, G.I., Weinberger, R., Marco, S., Levi, T., 2020c. Fold and thrust systems in mass transport deposits around the Dead Sea Basin. In: Ogata, K., Festa, A., Pini, G.A. (Eds.), Submarine Landslides: Subaqueous Mass Transport Deposits from Outcrops to Seismic Profiles. American Geophysical Union Monograph Series, vol. 246. John Wiley & Sons Inc, ISBN 978-1-119-50058-2, pp. 139–154, 384pp.
Arkin, Y., Michaeli, L., 1986. The significance of shear strength in the deformation of laminated sediments in the Dead Sea area. Isr. J. Earth Sci. 35, 61–72.
Armandita, C., Morley, C.K., Rowell, P., 2015. Origin, structural geometry, and the development of a giant slide: the South Makassar Strait mass transport complex. Geosphere 11, 376–403.
Bartov, Y., Steinitz, G., Eyal, M., Eyal, Y., 1980. Sinistral movement along the Gulf of Aqaba - its age and relation to the opening of the red Sea. Nature 285, 220–221.
Begin, Z.B., Ehrlich, A., Nathan, Y., 1974. Lake lisan, the Pleistocene precursor of the Dead Sea. Geol. Surv. Isr. Bull. 63, 30.
Ben Dor, Y., Neugebauer, I., Enzel, Y., Schwab, M.J., Tjallingii, R., Erel, Y., Brauer, A., 2019. Varves of the Dead Sea sedimentary record. Quat. Sci. Rev. 215, 173–184.
Boyer, S.E., 1992. Geometric evidence for synchronous thrusting in the southern Alberta and northwest Montana thrust belts. In: McClay, K. (Ed.), Thrust Tectonics. Chapman and Hall, London, pp. 377–390.
Bull, S., Cartwright, J., Huuse, M., 2009. A review of kinematic indicators from mass-transport complexes using 3D seismic data. Mar. Petrol. Geol. 26, 1132–1151.
Butler, R.W.H., 1982. The terminology of structures in thrust belts. J. Struct. Geol. 4, 239–245.
Butler, R.W.H., 2004. The nature of 'roof thrusts' in the Moine Thrust Belt, NW Scotland: implications for the structural evolution of thrust belts. J. Geol. Soc. 161, 1–11. London.
Butler, R.W.H., McCaffrey, W.D., 2004. Nature of thrust zones in deep water sand-shale sequences: outcrop examples from the Champsaur sandstones of SE France. Mar. Petrol. Geol. 21, 911–921.
Butler, R.W.H., Paton, D.A., 2010. Evaluating lateral compaction in deepwater fold and thrust belts: how much are we missing from "nature's sandbox"? GSA Today (Geol. Soc. Am.) 20, 4–10.
Corredor, F., Shaw, J.H., Bilotti, F., 2005. Structural styles in the deep-water fold and thrust belts of the Niger Delta. AAPG (Am. Assoc. Pet. Geol.) Bull. 89, 753–780.
Coward, M.P., Potts, G., 1983. Complex train patterns developed at the frontal and lateral tips to shear zones and thrust zones. J. Struct. Geol. 5, 383–399.
Dahlstrom, C.D.A., 1970. Structural geology in the eastern margin of the Canadian Rocky Mountains. Bull. Can. Petrol. Geol. 18, 332–406.
Debacker, T.N., Dumon, M., Matthys, A., 2009. Interpreting fold and fault geometries from within the lateral to oblique parts of slumps: a case study from the Anglo-Brabant Deformation Belt (Belgium). J. Struct. Geol. 31, 1525–1539.
de Vera, J., Granado, P., McClay, K., 2010. Structural evolution of the Orange Basin gravity-driven system, offshore Namibia. Mar. Petrol. Geol. 27, 223–237.
El-Isa, Z.H., Mustafa, H., 1986. Earthquake deformations in the Lisan deposits and seismotectonic implications. Geophys. J. Roy. Astron. Soc. 86, 413–424.
Elliot, D., 1976. The energy balance and deformation mechanisms of thrust sheets. Philos. Trans. R. Soc. London, Ser. A 283, 289–312.
Escher, A., Watterson, J., 1974. Stretching fabrics, folds and crustal shortening. Tectonophysics 22, 223–231.
Farrell, S.G., 1984. A dislocation model applied to slump structures, Ainsa Basin, South Central Pyrenees. J. Struct. Geol. 6, 727–736.
Farrell, S.G., Eaton, S., 1987. Slump strain in the Tertiary of Cyprus and the Spanish Pyrenees. Definition of palaeoslopes and models of soft sediment deformation. In: Jones, M.F., Preston, R.M.F. (Eds.), Deformation of Sediments and Sedimentary Rocks, vol. 29, pp. 181–196. Special Publication of the Geological Society of London.
Fischer, M.W., Coward, M.P., 1982. Strains and folds within thrust sheets: an analysis of the Heilam sheet, northwest Scotland. Tectonophysics 88, 291–312.
Fossen, H., 2016. Structural Geology, second ed. Cambridge University Press, Cambridge, UK, p. 510.
Frey Martinez, J., Cartwright, J., Hall, B., 2005. 3D seismic interpretation of slump complexes: examples from the continental margin of Israel. Basin Res. 17, 83–108.
Frey-Martinez, J., Cartwright, J., James, D., 2006. Frontally confined versus frontally emergent submarine landslides: a 3D seismic characterisation. Mar. Petrol. Geol. 23, 585–604.
Frydman, S., Charrach, J., Goretsky, I., 2008. Geotechnical properties of evaporite soils of the Dead Sea area. Eng. Geol. 101, 236–244.
Garcia-Tortosa, F.J., Alfaro, P., Gibert, L., Scott, G., 2011. Seismically induced slump on an extremely gentle slope (<1°) of the Pleistocene Tecopa paleolake (California). Geology 39, 1055–1058.
Garfunkel, Z., 1981. Internal structure of the Dead Sea leaky transform (rift) in relation to plate kinematics. Tectonophysics 80, 81–108.
Garfunkel, Z., Ben-Avraham, Z., 1996. The structure of the Dead Sea basin. Tectonophysics 26, 155–176.
Gibert, L., Sanz de Galdeano, C., Alfaro, P., Scott, G., Lopez Garrido, A.C., 2005. Seismic-induced slump in early Pleistocene deltaic deposits of the Baza basin (SE Spain). Sediment. Geol. 179, 279–294.
Haase-Schramm, A., Goldstein, S.L., Stein, M., 2004. U-Th dating of Lake Lisan aragonite (late Pleistocene Dead Sea) and implications for glacial East Mediterranean climate change. Geochem. Cosmochim. Acta 68, 985–1005.
Haliva-Cohen, A., Stein, M., Goldstein, S.L., Sandler, A., Starinsky, A., 2012. Sources and transport routes of fine detritus material to the late quaternary Dead Sea basin. Quat. Sci. Rev. 50, 55–70.
Heifetz, E., Agnon, A., Marco, S., 2005. Soft sediment deformation by Kelvin Helmholtz instability: a case from Dead Sea earthquakes. Earth Planet Sci. Lett. 236, 497–504. https://doi.org/10.1016/j.epsl.2005.04.019.
Jablonska, D., Di Celma, C., Tondi, E., Alsop, G.I., 2018. Internal architecture of mass-transport deposits in basinal carbonates: a case study from southern Italy. Sedimentology 65 (4), 1246–1276. https://doi.org/10.1111/sed.12420.
Jackson, C.A.-L., 2011. Three-dimensional seismic analysis of megaclast deformation within a mass transport deposit: implications for debris flow kinematics. Geology 39, 203–206.
Jacoby, Y., Weinberger, R., Levi, T., Marco, S., 2015. Clastic dikes in the Dead Sea Basin as indicators to potential hazard. Nat. Hazards 75, 1649–1676. https://doi.org/10.1007/s11069-014-1392-0.
Jelinek, V., 1981. Characterization of magnetic fabric of rocks. Tectonophysics 79, 63–67.
Jolly, B.A., Lonergan, L., Whittaker, A.C., 2016. Growth history of fault-related folds and interaction with seabed channels in the toe-thrust region of the deep-water Niger delta. Mar. Petrol. Geol. 70, 58–76.
Kagan, E.J., Stein, M., Marco, S., 2018. Integrated palaeoseismic chronology of the last glacial Lake Lisan: from lake margin seismites to deep-lake mass transport deposits. J. Geophys. Res.: Solid Earth 123 (4), 2806–2824.
Korneva, I., Tondi, E., Jablonska, D., Di Celma, C., Alsop, I., Agosta, F., 2016. Distinguishing tectonically- and gravity-driven synsedimentary deformation structures along the Apulian platform margin (Gargano Promontory, southern Italy). Mar. Petrol. Geol. 73, 479–491.
Levi, T., Weinberger, R., Aïfa, T., Eyal, Y., Marco, S., 2006a. Injection mechanism of clay-rich sediments into dikes during earthquakes. G-cubed 7, Q12009–12. https://doi.org/10.1029/2006GC001410.
Levi, T., Weinberger, R., Aïfa, T., Eyal, Y., Marco, S., 2006b. Earthquake-induced clastic dikes detected by anisotropy of magnetic susceptibility. Geology 34 (2), 69–72.
Levi, T., Weinberger, R., Eyal, Y., Lyakhovsky, V., Hefez, E., 2008. Velocities and driving pressures of clay-rich sediments injected into clastic dykes during earthquakes. Geophys. J. Int. 175, 1095–1107.
Levi, T., Weinberger, R., Marco, S., 2014. Magnetic fabrics induced by dynamic faulting reveal damage zone sizes in soft rocks, Dead Sea basin. Geophys. J. Int. 199 (2), 1214–1229.
Levi, T., Weinberger, R., Alsop, G.I., Marco, S., 2018. Characterizing seismites with anisotropy of magnetic susceptibility. Geology 46 (9), 827–830.
Lu, Y., Waldmann, N., Alsop, G.I., Marco, S., 2017. Interpreting soft sediment deformation and mass transport deposits as seismites in the Dead Sea depocentre. J. Geophys. Res.: Solid Earth 122, 8305–8325. https://doi.org/10.1002/2017JB014342, 10.
Maltman, A., 1984. On the term soft-sediment deformation. J. Struct. Geol. 6, 589–592.
Marco, S., Agnon, A., 1995. Prehistoric earthquake deformations near Masada, Dead Sea graben. Geology 23, 695–698.
Marco, S., Stein, M., Agnon, A., Ron, H., 1996. Long term earthquake clustering: a 50,000 year paleoseismic record in the Dead Sea Graben. J. Geophys. Res. 101, 6179–6192.
Morley, C.K., King, R., Hillis, R., Tingay, M., Backe, G., 2011. Deepwater fold and thrust belt classification, tectonics, structure and hydrocarbon prospectivity: a review. Earth Sci. Rev. 104, 41–91.
Nuriel, P., Weinberger, R., Kylander-Clark, A.R.C., Hacker, B.R., Cradock, J.P., 2017. The onset of the Dead Sea transform based on calcite age-strain analyses. Geology 45, 587–590.
Ogata, K., Mountjoy, J.J., Pini, G.A., Festa, A., Tinterri, R., 2014. Shear zone liquefaction in mass transport deposit emplacement: a multi-scale integration of seismic reflection and outcrop data. Mar. Geol. 356, 50–64.
Parés, J.M., 2015. Sixty years of anisotropy of magnetic susceptibility in deformed sedimentary rocks. Front. Earth Sci. 3, 4.
Peel, F.J., 2014. The engines of gravity-driven movement on passive margins: quantifying the relative contribution of spreading vs. gravity sliding mechanisms. Tectonophysics 633, 126–142.
Porat, N., Levi, T., Weinberger, R., 2007. Possible resetting of quartz OSL signals during earthquakes – evidence from late Pleistocene injection dikes, Dead Sea basin, Israel. Quat. Geochronol. 2, 272–277.
Prasad, S., Negendank, J.F.W., Stein, M., 2009. Varve counting reveals high resolution radiocarbon reservoir age variations in palaeolake Lisan. J. Quat. Sci. 24, 690–696.
Rees, A.I., 1966. The effects of depositional slopes on the anisotropy of magnetic susceptibility of laboratory deposited sands. J. Geol. 74, 856–867.
Reis, A.T., Araújo, E., Silva, C.G., Cruz, A.M., Gorini, C., Droz, L., Migeon, S., Perovano, R., King, I., Bache, F., 2016. Effects of a regional décollement level for gravity tectonics on late Neogene to recent large-scale slope instabilities in the Foz do Amazonas Basin, Brazil. Mar. Petrol. Geol. 75, 29–52.
Ron, H., Nowaczyk, N.R., Frank, U., Marco, S., McWilliams, M.O., 2006. Magnetic properties of Lake Lisan and Holocene Dead Sea sediments and the fidelity of chemical and detrital remnant magnetization. Geol. Soc. Am. Spec. Pap. 401, 171–182.

Scarselli, N., McClay, K., Elders, C., 2016. Seismic geomorphology of Cretaceous megaslides offshore Namibia (Orange Basin): insights into segmentation and degradation of gravity-driven linked systems. Mar. Petrol. Geol. 75, 151–180.
Sharman, G.R., Graham, S.A., Masalimova, L.U., Shumaker, L.E., King, P.R., 2015. Spatial patterns of deformation and palaeoslope estimation within the marginal and central portions of a basin-floor mass-transport deposit, Taranaki Basin, New Zealand. Geosphere 11, 266–306.
Smit, J., Brun, J.-P., Fort, X., Cloetingh, S., Ben-Avraham, Z., 2008. Salt tectonics in pull-apart basins with application to the Dead Sea Basin. Tectonophysics 449, 1–16.
Sneh, A., Bartov, Y., Weissbrod, T., Rosenaft, M., 1998. Geological Map of Israel, Scale 1: 200,000. Geological Survey of Israel, Jerusalem.
Sneh, A., Weinberger, R., 2014. Major Structures of Israel and Environs, Scale 1:500,000. Israel Geological Survey, Jerusalem.
Sobiesiak, M., Kneller, B.C., Alsop, G.I., Milana, J.P., 2017. Sub-seismic scale folding and thrusting within an exposed mass transport deposit: a case study from NW Argentina. J. Struct. Geol. 96, 176–191.
Steventon, M.J., Jackson, C.A.-L., Hodgson, D.M., Johnson, H.D., 2019. Strain analysis of a seismically imaged mass-transport complex, offshore Uruguay. Basin Res. 31, 600–620.
Strachan, L.J., Alsop, G.I., 2006. Slump folds as estimators of palaeoslope: a case study from the Fisherstreet Slump of County Clare, Ireland. Basin Res. 18, 451–470.
Torfstein, A., Haase-Schramm, A., Waldmann, N., Kolodny, Y., Stein, M., 2007. U-Th, delta O-18 and paleomagnetic dating of a mid-Pleistocene lacustrine sequence: the Amora Formation, Mount Sedom, Israel. Geochem. Cosmochim. Acta 71 (15). A1031–A1031.
Totake, Y., Butler, R.W.H., Bond, C.E., Aziz, A., 2018. Analyzing structural variations along strike in a deep-water thrust belt. J. Struct. Geol. 108, 213–229. https://doi.org/10.1016/j.jsg.2017.06.007.
Van der Merwe, W.C., Hodgson, D.M., Flint, S.S., 2011. Origin and terminal architecture of a submarine slide: a case study from the Permian Vischkuil Formation, Karoo Basin, South Africa. Sedimentology 58, 2012–2038.
Watkins, H., Butler, R.W.H., Bond, C.E., 2017. Using laterally compatible cross sections to infer fault growth and linkage models in foreland thrust belts. J. Struct. Geol. 96, 102–117.
Weinberger, R., Levi, T., Alsop, G.I., Eyal, Y., 2016. Coseismic horizontal slip revealed by sheared clastic dikes in the Dead Sea basin. Geol. Soc. Am. Bull. 128, 1193–1206.
Weinberger, R., Levi, T., Alsop, G.I., Marco, S., 2017. Kinematics of mass transport deposits revealed by magnetic fabrics. Geophys. Res. Lett. 44, 7743–7749.
Wetzler, N., Marco, S., Heifetz, E., 2010. Quantitative analysis of seismogenic shear-induced turbulence in lake sediments. Geology 38 (4), 303–306. https://doi.org/10.1130/G30685.1.
Woodcock, N.H., 1976a. Ludlow series slumps and turbidites and the form of the montgomery trough, Powys, Wales. Proc. Geol. Assoc. 87, 169–182.
Woodcock, N.H., 1976b. Structural style in slump sheets: Ludlow series, Powys, Wales. J. Geol. Soc. 132, 399–415. London.
Woodcock, N.H., 1979. The use of slump structures as palaeoslope orientation estimators. Sedimentology 26, 83–99.
Xypolias, P., Alsop, G.I., 2014. Regional flow perturbation folding within an exhumation channel: a case study from the Cycladic blueschists. J. Struct. Geol. 62, 141–155.
Zalan, P.V., 2005. End members of gravitational fold and thrust belts (GFTBs) in the deep waters of Brazil. In: Shaw, J.H., Connors, C., Suppe, J. (Eds.), An AAPG Seismic Atlas: AAPG Studies in Geology, vol. 53, pp. 147–156.